Spring 2018

2D and 3D control of photopolymerized polycaprolactone scaffolds for cell replacement therapy in retinal disease

Jessica Rae Thompson
University of Iowa

2D AND 3D CONTROL OF PHOTOPOLYMERIZED POLYCAPROLACTONE SCAFFOLDS FOR CELL REPLACEMENT THERAPY IN RETINAL DISEASE

by

Jessica Rae Thompson

A thesis submitted in partial fulfillment
of the requirements for the Master of Science
degree in Biomedical Engineering in the
Graduate College of
The University of Iowa

May 2018

Thesis Supervisors: Associate Professor Budd A. Tucker
Assistant Professor Kristan S. Worthington

Graduate College
The University of Iowa
Iowa City, Iowa

CERTIFICATE OF APPROVAL

_____

MASTER'S THESIS

_____

This is to certify that the Master's thesis of

Jessica Rae Thompson

has been approved by the Examining Committee for
the thesis requirement for the Master of Science degree
in Biomedical Engineering at the May 2018 graduation.

Thesis Committee: _____
Budd A. Tucker, Thesis Supervisor

_____
Kristan S. Worthington, Thesis Supervisor

_____
James A. Ankrum

_____
Luke A. Wiley

This thesis is dedicated to my parents and grandparents for all their emotional and financial support throughout my education.

ABSTRACT

Obstacles to the realization of polymer scaffolds to be used for cell replacement therapies often include the challenges in controlling the microstructure of biocompatible molecules in three dimensions at cellular scales. Two-photon polymerization (TPP) of acrylated poly(caprolactone) (PCL) offers a means of achieving precise microstructural control of a material in a biocompatible and biodegradable platform. Two obstacles inhibit the efficient development and research of this method: there is not a commercially available acrylated PCL and the fabrication time using TPP can be lengthy. Initially in this work, TPP parameters and molecular structures were varied to find the ideal relationship for our prototype. Increasing the concentration of reactive groups, either by increasing number of acrylate groups per molecule or decreasing molecular weight, was found to increase the similarity of the scaffold to the computer generated model. Sub-retinal implantation of TPP PCL scaffolds in a porcine model of retinitis pigmentosa was well tolerated, and did not cause inflammation, infection, or local or systemic toxicity after one month. However, this acrylated PCL was not as pure as originally thought; there were remaining reactants present that prevented accurate quantification of reaction success. Without the ability to measure the number of acrylates that were bonded to the molecule we could not ensure that batches were consistent, preventing a standard to be developed for quality and control. A method to purify the products of our PCL synthesis was delineated; a series of washes and separations with concentrated sodium bicarbonate successfully purified the PCL. The more thoroughly the phases were combined during these washes, the more effectively the reactant was removed. To address the time scale issues of TPP, the implementation of a two-dimensional photo-masked (PM) polymerized

PCL film was adopted. Since films are faster and simpler to make, they can be developed and tested first and used as a predicate device for FDA approval of TPP PCL scaffolds. Therefore, the PM scaffolds were formulated similarly to the TPP materials and then the minimum intensity of light and time necessary to polymerize a film was determined. Time and light intensity displayed an inverse relationship, and the films at each intensity and exposure require more research into their quality and elastic modulus . A representative film was selected, seeded with dissociated retinal organoids, and, after one week, the cells that successfully adhered to the scaffold maintained their neuronal lineage. The density of cells seeded using 16 retinal organoids was estimated and will provide insight into how many organoids to use in the future. These results represent an important step towards understanding how photopolymerization can be applied to a wide range of biologically compatible chemistries for various biomedical applications.

PUBLIC ABSTRACT

Millions of people suffer from blinding diseases like age-related macular degeneration or retinitis pigmentosa. Current treatments for these disorders only slow the progression of disease. In order to restore vision of patients, we propose to deliver patient-derived, immature, light-sensing cells into the eye using a polymer support. This work focuses on using high-resolution 3D printing to make intricately structured tissue scaffolds with a degradable polymer (a.k.a. plastic). Since the starting material cannot be purchased, our first step was to develop a method for reliable polymer production. Then, chemical properties of the plastic and the settings of the printer were varied to determine the ideal parameters for creating our desired structures. Our preliminary studies in animals show that the 3D-printed structures are non-toxic to the eye. However, the high-resolution 3D printing technique we used can be prohibitively slow, so we refined a separate, more rapid fabrication technique. While equally safe in preliminary animal studies, this technique does not offer the same level of resolution as the first. Overall, our results delineate the advantages and disadvantages of each method. Together, our findings set the stage for the ability to transplant rods and cones to patients suffering from previously incurable blindness.

TABLE OF CONTENTS

List of Tables viii

List of Figures ix

Chapter I: Introduction 1

1.1 Purpose 1

1.2 Cell Replacement Therapy 1

1.3 Retinal Biomaterials 2

1.4 Retinal Biomaterial Structure 4
1.4.1 Solvent Casting 4
1.4.2 Fiber Casting 5
1.4.3 Photopolymerization 5

1.5 Objectives 6

Chapter II: Two-Photon Three Dimensional Printed Scaffold 7

2.1 Introduction 7

2.2 Methods 7
2.2.1 PCL Functionalization 7
2.2.2 Formulation 8
2.2.3 Sample Preparation 9
2.2.4 Scanning Electron Microscopy 10
2.2.5 Threshold and Resolution 10
2.2.6 Scaffold Fidelity to Model 11
2.2.7 Scale-Up Optimization 12
2.2.8 *In vivo* Biocompatibility 13
2.2.9 Statistical Analyses 14

2.3 Results 16
2.3.1 Determination of Printing Thresholds 16
2.3.2 Determination of Print Resolution 19
2.3.3 Analysis of Model to Scaffold Fidelity 21
2.3.4 Scale-Up Optimization 31
2.3.5 *In vivo* Biocompatibility 33

2.4 Discussion 35

2.5 Supplemental Information 39
2.5.1 Supplemental Materials and Methods 39
2.5.2 Figures 41
2.5.3 Tables 50

Chapter III: Purification of Acrylated PCL 63

3.1 Introduction 63

3.2 Methods 64
3.2.1 PCL Functionalization 64

3.2.2 PCL Purification 64
3.2.3 Reaction Validation and Analysis 65
3.3 Results 66
3.3.1 Method of Reactant Removal 66
3.3.2 Method of Agitation 69
3.4 Discussion 70
3.5 Supplemental Information 73
Chapter IV: UV Polymerized Two Dimensional Scaffolds 74
4.1 Introduction 74
4.2 Methods 75
4.2.1 Photomasked Film Fabrication 75
4.2.2 Dynamic Mechanical Analysis 77
4.2.3 Confocal Microscopy 77
4.2.4 Scaffold Preparation and Cell Loading 78
4.3 Results 80
4.3.1 Threshold 80
4.3.2 Pore Analysis 82
4.4 Discussion 85
4.5 Supplemental Information 89
Chapter V: Conclusions and Future Directions 90
5.1 Conclusions 90
5.2 Future Directions and Recommendations 92
References 96

LIST OF TABLES

Table 2.1: Optimal scanning speeds and laser powers for PCLTA formulations with 3 wt% photoinitiator. 21

Table 2.S1: Statistical analyses of the effects of slicing distance, hatching distance, molecular weight and polymer concentration on scaffold width. 50

Table 2.S2: Statistical analyses of the effects of slicing distance, hatching distance, molecular weight and polymer concentration on vertical pore diameter. 53

Table 2.S3: Statistical analyses of the effects of slicing distance, hatching distance, molecular weight and polymer concentration on scaffold height. 55

Table 2.S4: Statistical analyses of the effects of slicing distance, hatching distance, molecular weight and polymer concentration on vertical pore roundness. 59

Table 2.S5: Statistical analyses of the effects of slicing distance, hatching distance, molecular weight and polymer concentration on horizontal pore quality. 61

Table 2.S6: List of tissues harvested and examined for evaluation of systemic toxicity and tumorigenicity. 62

LIST OF FIGURES

Figure 2.1. Two-photon polymerization threshold. 17

Figure 2.2: Determining optimal laser power and scanning speed. 20

Figure 2.3: Influence of slicing distance, hatching distance and molecular weight on scaffold width..... 22

Figure 2.4: Influence of molecular weight and prepolymer concentration on the vertical pore diameter of PCLTA scaffolds. 26

Figure 2.5: Scale-up of optimized two-photon polymerization to transplantation-relevant size. 32

Figure 2.6: Scaled-up prototype of crosslinked PCLTA 900 in the degenerating pig sub-retinal space 30 days after transplantation. 34

Figure 2.S1: Representative Validation of Acrylation with Nuclear Magnetic Resonance Imaging. 41

Figure 2.S2: Schematic of process used to calculate the height of truncated hexagonal pyramid scaffolds. 42

Figure 2.S3: Pore quality scale used to compare horizontal pores. The quantitative scale used to rate and describe the horizontal pore quality. The scale bar represents 10 μm. 43

Figure 2.S4: Influence of slicing distance, hatching distance and molecular weight on scaffold height. 44

Figure 2.S5: Influence of molecular weight and prepolymer concentration on vertical pore roundness. 46

Figure 2.S6: Influence of slicing distance, hatching distance, molecular weight and prepolymer concentration on horizontal pore quality. 48

Figure 2.S7: Reproducibility of two-photon polymerized scaffolds. 49

Figure 3.1: Integration of acrylate peaks relative to methyl peaks. 67

Figure 3.2: Chemical shifts and sample purity. 68

Figure 3.S1: Improved substitution of acrylates. 73

Figure 4.1: Thresholds and compressive modulus. 81

Figure 4.2: Confocal microscopy and pore profiles. 83

Figure 4.3: PM PCLTA loaded with retinal organoids. 84

Figure 4.S1: Complete comparison of PM PCLTA pores. 89

CHAPTER I: INTRODUCTION

1.1 Purpose

Millions of individuals have been diagnosed with disorders that cause retinal degeneration, resulting in a currently irreversible loss of vision. These patients experience a reduction in their quality of life as their vision dissipates and are more likely to experience depression than their sighted peers.[1] One of the largest causes of blindness is age-related macular degeneration (AMD), and this disorder, like many others, only has treatments that can slow the progression of disease, not restore sight.[2-3] This work focuses on the design of a polymeric scaffold to boost the efficacy of cell replacement therapies and thus offers a potential improvement in the prognosis of retinal degeneration.

1.2 Cell Replacement Therapy

As more extensive research emerges on the use of induced pluripotent stem cells (iPSCs) for tissue regeneration, there is hope that cell replacement therapy will be a viable treatment option to restore vision. The cells that detect light, the photoreceptor cells, are the most critical of those damaged during retinal degeneration. No matter the cause of the disorder resulting in blindness (i.e., genetic vs. environmental), visual restoration would require the delivery of healthy cells to the retina in cases where rods and cones have died. The use of donor tissue or cells could necessitate expensive and potentially harmful immunosuppression for life, which leaves patients highly susceptible to infections. In contrast, the use of autologous cells and tissues with genetic modification, if needed, would allow patients to maintain their natural immune system. With recent advances in techniques that can be used to manipulate human induced

pluripotent stem cells (hiPSCs) genomes,[4] such as clustered regularly interspaced short palindromic repeats (CRISPR) and CRISPR-associated nucleases (Cas), this genetic engineering of patient-specific tissue is a possibility.[5-6] However, an efficient mechanism of delivery to the retina has yet to be determined; simple bolus injection of the cells into the subretinal space results in poor cell survival and integration in a last-stage degenerate retina mouse model. Injections may have unsatisfactory outcomes because the shear forces applied to the cells, and/or there is not enough remaining retina tissue to indicate appropriate incorporation of cells into the eye. The use of a polymeric delivery vehicle increases the rate of cell survival upon transplantation.[7-8] Additionally, with the right selection of biomaterial and scaffold structure, a polymer substrate can enable cell alignment in the tissue and support,

1.3 Retinal Biomaterials

An effective material for a photoreceptor cell tissue scaffold would ideally mimic the native tissue. First, a biocompatible material is desirable because if it elicits an immune response it would cause more damage to the already sensitive retina. The device should also have a structure that facilitates integration into the host tissue. Furthermore, the biomaterial would ideally have an elastic modulus similar to that of the retina, on the scale of 10-20 kPa.[9] Finally, the degradation of the vehicle should be timely, on the scale of 2 to 3 months, and the dissolution products should leave no lasting impact on the retina.

To date, several polymers have been investigated pre-clinically as retinal cell delivery scaffolds, including commercially available poly(lactic-co-glycolic acid) (PLGA),[10] poly(lactic acid) (PLA),[10] poly(methyl methacrylate) (PMMA),[11]

poly(glycerol-sebacate) (PGS),[12] and poly(caprolactone) (PCL). [13-14] Each of these materials has advantages and disadvantages. For example, PMMA-based scaffolds, while typically well-tolerated in the eye, are non-biodegradable and can lead to tissue damage including post-transplant retinal detachment.[11, 14] Similarly, biodegradable scaffolds made from polymers such as PLGA and PLA, which have been widely used in production of microspheres for ocular drug delivery,[15-17] are often rigid and brittle,[17-18] making them difficult to manipulate surgically and mechanically incompatible with the host retina once transplanted.[9] Furthermore, PLGA/PLA based scaffolds, which typically undergo rapid bulk degradation, release acidic degradation products that are locally toxic and can cause severe post-transplant inflammation.[10]

Poly(caprolactone) is a degradable polyester that has been used extensively in several biomedical applications including drug delivery, sutures, and tissue scaffolds.[19-20] PCL is often used because of its biologically favorable rheological and viscoelastic properties, which make it relatively easy to manipulate into scaffolds and structures with a wide range of properties.[21-23] Additionally, PCL is well tolerated in part because of its slow degradation time, leading to no pathologic increase in local acidity.[14, 24] While surface patterned PCL has been used to organize and differentiate murine retinal progenitor cells *in vitro*,[13] additional three-dimensional (3D) control of the scaffold structure is necessary to customize this material for human retinal cell replacement therapies.

1.4 Retinal Biomaterial Structure

To achieve the desired structure of the biomaterials previously mentioned, there are a number of fabrication techniques used to date with varying degrees of control and microstructure.

1.4.1 Solvent Casting

A basic casting features a fluid entering a mold and solidifying, resulting in the material taking on the negative of the cast's features. In order to add more complexity to materials, there are multiple modifications of simple casting techniques. A specialized case of solvent casting, the breath figure method uses a polymer dissolved in an organic solvent and is exposed to a humid environment. As the water droplets condensate on the surface of the organic phase, the solvent evaporates. Once all the solvent evaporates, the polymer keeps the shape of the water droplets that formed on the surface. Retinal scaffolds manufactured with this method and coated with collagen were able to demonstrate pore sizes as low as about 5 μm, allowing small molecules to flow through the membrane but not cells.[25] Similarly, controlled phase separation takes advantage of the freezing point of the solvent via sublimation it off, leaving only (in this case) a PLGA and PLA scaffold with 35-50 μm porous structure.[10] Although this copolymer successfully increased the number of cells delivered to the subretinal space in animal models, the material was too brittle to fold and compact for less invasive surgery. These casting methods allow for the size of pores to be varied to an extent, but the depth of the pore and thus total allowable scaffold thickness cannot be readily controlled.

1.4.2 Fiber Casting

Another method of producing polymer structures with microstructure that have been studied includes spin casting. In this technique, a polymer in a fluid state is extruded through a spinneret onto a surface and allowed to solidify. In a process known as electrospinning, an electric charge is used to draw out the polymer, which results in fibers with semi-controllable dimensions on the scale of micro- and nanometers. Electrospun porous PLGA and poly (L-lactide-co-caprolactone) (PLCL) have been studied as substrates to transplant cells to the subretinal space.[15, 26] Similar to the solvent cast structures, electrospinning creates a penetrable membrane on which cells rest and small molecules can pass through. These designs are suitable for the retinal pigmented epithelium because they form a simple, single layer and must have access to nutrients. However, cells that require appropriate multi-layered, three-dimensional structure to function properly will need more support from a biomaterial.

1.4.3 Photopolymerization

Photopolymerization functions on the principal that a photon of light activates a photoinitiator to form a free radical. When this free radical is in a solution with monomer or prepolymer subunits containing carbon-carbon double bonds, it reacts with these electrophilic functional groups. The free radical opens the double bond and is then transferred to the monomer or prepolymer molecule, where it continues propagating the polymerization reaction by attacking new monomer molecules throughout the solution. For the purpose of this work, there are two categories of photopolymerization: UV polymerization and two-photon polymerization. During UV polymerization, light will cause polymerization of a sample (often resulting in a liquid to solid transition) anywhere

that it encounters photoinitiator and monomer together (i.e. every illuminated spot in the sample). In two-photon polymerization, a wavelength of light is selected such that it produces photons that each have half the energy necessary to excite the photoinitiator. This light source (typically a laser) is focused through an objective lens. Only in the location where two photons collide will a photoinitiator activate and begin the polymerization chain reaction. This results in precise control of where the polymerization will occur and allows for three dimensional control of a desired biomaterial in high resolution (<100 nm). Fabrication of a 3D tissue scaffold has been achieved using this technique with a commercial resin that is not biocompatible.[27] Despite the drawbacks of the chemical composition of these prototypes, human retinal progenitor cells were seeded on this 3D printed scaffold and after two-days neuronal processes extended into the pores. Thus, the technology holds great promise for creating intricately structured and designed biomaterials in three dimensions.

1.5 Objectives

On the basis of previously described recommendations for material chemistry and foundational knowledge about various microstructuring techniques, this study aims to explore photopolymerization of polycaprolactone to generate a biocompatible photoreceptor cell replacement scaffold. Polycaprolactone has been established as a suitable material in the ocular environment and has favorable degradation and mechanical properties. Furthermore, photopolymerization, particularly two-photon, allows for precise microstructural control of a biomaterial. By harnessing the potential of photopolymerization to create structured PCL, we aim to create a superior retinal tissue scaffold in pursuit of effective retinal degeneration treatments.

CHAPTER II: TWO-PHOTON THREE DIMENSIONAL PRINTED SCAFFOLD

2.1 Introduction

In this work, we describe the potential of two-photon lithography for high resolution photopolymerized PCL microstructures and evaluated factors that optimize these materials for retinal cell replacement therapies. We modified PCL with acrylate groups at varying degrees of functionality and molecular weight, while also evaluating the effect of PCL and photoinitiator concentration. Importantly, the addition of acrylate groups allowed PCL to undergo photopolymerization, enabling spatial and temporal control of the resulting structure. For each formulation, we varied laser scanning speed and power to determine the two-photon polymerization threshold. At fixed and optimized two-photon scanning speed and laser power for each formulation, we also varied the hatching and slicing distances of the modeled scaffolds to study design-to-structure fidelity and the ability to scale-up to translationally relevant scaffolds. Lastly, we evaluated scaffold biocompatibility via sub-retinal implantation in a pig model of inherited retinal degeneration. Collectively, these results lay the groundwork for applying two-photon polymerization to degradable polymer systems for applications such as retinal regeneration where precise control of material micro-architecture is required.

2.2 Methods

2.2.1 PCL Functionalization

PCL diol (530, 1250 and 2000 g/mol) and PCL triol (300 and 900 g/mol) (Sigma-Aldrich, St. Louis, MO) were used after being dried at 110 °C overnight and cooled under vacuum. Potassium carbonate (KCO3, Fisher Scientific, Hampton, NH) was used after being dried at 110 °C for 24 hours. Acryloyl chloride and dichloromethane (Sigma-

Aldrich) were used as received. PCL diol and triol of varying molecular weights were functionalized using a modified protocol based on established methods described elsewhere.34 Approximately 10 g of PCL were dissolved in 100 mL dichloromethane. A slurry was formed when potassium carbonate was added at a 1.5 molar ratio with respect to the PCL alcohol groups. In a separate container, acryloyl chloride equimolar to the KCO3 was dissolved in dichloromethane (1:5 v/v). The reaction flask was purged with argon gas for 10 minutes before the acryloyl chloride solution was added dropwise while stirring. The reaction proceeded at room temperature for 24 hours under argon. After completion of the reaction, the mixture was filtered to remove the solids and the resulting solution was rotary-evaporated, leaving the functionalized PCL as a waxy solid or viscous liquid, depending on the molecular weight.

Acrylation of PCL was confirmed via 1H nuclear magnetic resonance (NMR) imaging. After purification, each functionalized PCL was dissolved in deuterated chloroform (Sigma-Aldrich) and the solutions were analyzed using a Bruker Avance-300 probe with a field strength of 300 MHz (Figure 2.S1). For the purposes of this manuscript, acrylated PCL diol and PCL triol will be referred to as PCL diacrylated (PCLDA) and PCL triacrylate (PCLTA), respectively.

2.2.2 Formulation

To prepare samples for photopolymerization, functionalized PCL prepolymers were dissolved in dioxane (Sigma-Aldrich) to form PCL:dioxane solutions (Ratios of 3:1, 1:1, 1:3). A photoinitiator, 2-Benzyl-2-dimethylamino-1-(4-morpholinophenyl)-butanone-1 (commonly known as Irgacure 369 or I-369, Ciba Specialty Chemicals, BASF, Ludwigshafen, Germany) was added to the solution (at 1, 3 , and 5 wt%).

2.2.3 Sample Preparation

3D models were created in AutoCAD 2015 (Autodesk Inc., San Rafael, CA). DeScribe version 2.2.1 (Nanoscribe GmbH; Eggenstein-Leopoldshafen, Germany) was used to slice and hatch the models. The resulting code file was used to vary laser power and scanning speed. To facilitate structure adhesion to the substrate, 30 mm glass coverslips were exposed to oxygen plasma (Plasma Cleaner PCD-001 equipped with PlasmaFlo gas flow control; Harrick Plasma; Ithaca, NY) at an oxygen flow rate of 22.5 mL/min at 30 W radio frequency power for three minutes. Following this surface activation, coverslips were soaked in a 1% solution of 3-(trimethoxysilyl)propyl methacrylate (Sigma-Aldrich) in hexanes (Fisher Scientific) for 2-3 hours. The coverslips were rinsed in fresh hexanes and dried overnight. The functionalized substrate was secured to the sample holder, and a drop of oil (Immersol 518 F, Carl Zeiss; Inc Oberkochen, Germany) was applied to the uncoated side. To prevent undesirable sample migration and evaporation, vacuum grease was applied to a stainless steel washer (1.5cm O.D., 0.75cm I.D.) and placed in the center of the coated side of a glass substrate. The resulting well was filled dropwise with the prepolymer solution and, if the solution was particularly prone to evaporation, a non-coated glass coverslip was placed over the washer. The sample holder was inserted into the Nanoscribe Photonic Professional GT two-photon lithography system (Nanoscribe GmbH), and the designated structure was printed using regular 3D direct-laser-writing and a 25X objective (NA = 0.8). Once printing was complete, the substrate was removed from the sample holder, and the washer and vacuum grease were carefully removed from the substrate. To remove the

unreacted prepolymer, the sample, still attached to the substrate, was soaked in 1,4-dioxane overnight and then dried at room temperature.

2.2.4 Scanning Electron Microscopy

Two-photon polymerized samples were coated with a gold-palladium mixture using an argon beam K550 sputter coater (Emitech Ltd.; Kent, England). Images were collected with a 1.0kV accelerating voltage at suitable magnifications for the model size using a Hitachi S-4800 scanning electron microscope (Hitachi High-Technologies; Ontario, Canada). For scaffolds, images were also collected with a 30° tilt applied to the stage.

2.2.5 Threshold and Resolution

A 10 μm wide (point-to-point) by 1 μm tall star was designed with a 0.1 μm slicing distance and 0.1 μm hatching distance. Based on previously published optimizations, hatching type was fixed as parallel lines with the direction alternating by 90° between each layer.[28] For each formulation, attempts to form this star were performed using laser power ranging from 2% to 100% in increments of 2% and scanning speeds ranging from 6 mm/s to 40 mm/s in increments of 2 and 60 mm/s to 160 mm/s in increments of 20 mm/s. The presence of the stars was determined qualitatively. The minimum laser power at which a star was present was deemed the polymerization threshold. At the fastest scanning speed that did not result in undesirable artifacts, the width (point-to-point) of each star near the polymerization threshold was measured in triplicate using image analysis (ImageJ 1.48v) of scanning electron micrographs.

2.2.6 Scaffold Fidelity to Model

Generic scaffolds were designed as previously described.[28] Briefly, each scaffold had 20 μm diameter vertical pores intended to house cells and 7 μm diameter horizontal pores intended to allow fluid and nutrient transport. For each formulation, the optimum scanning speed and laser power were selected based on the conditions that resulted in stars with widths closest to the model (see experimental design above). The slicing distance was held constant at 0.5 μm while the hatching distance was manipulated: 0.1, 0.5, 1.0, and 1.5 μm. Likewise, the hatching distance was held constant at 0.5 μm while the slicing distance was manipulated: 0.1, 0.5, 1.0, and 1.5 μm. The diameter and roundness of the vertical pores, as well as the scaffold width and height, were evaluated using SEM and ImageJ. Briefly, ImageJ was used to create binary versions of the top-down (non-tilted) SEM images using the threshold function and then the Analyze Particles function was used to find the area (A) and roundness (R) of the pores. Pore diameter (D) and roundness were calculated as follows:

$$D = 2\sqrt{A/\pi}$$

$$R = \frac{4A}{\pi(Mj)^2}$$

where Mj is the major axis of the pore, as measured by the Analyze Particles function.

The top width of each scaffold was measured in triplicate from the non-tilted images for each scaffold. A single measurement of scaffold width at the substrate interface was also collected from these measurements. Three measurements of perceived scaffold height were measured from images collected after the samples had been tilted 30

degrees. These measurements, together with scaffold width measurements, were used to calculate actual scaffold height, as described further in the Supplemental Information (**Figure 2.S2**).

The quality of the horizontal pores was determined using a 4-point scale (0 – 3) with zero representing a complete absence of pores and three representing pores that appeared to traverse the full width of the scaffold, see **Figure 2.S3** for visual representation of quality rankings. For each scaffold, a single value was assigned to each layer of horizontal pores for a total of three observations per scaffold.

To better understand the reproducibility of this fabrication process, triplicate sets of scaffolds with varying slicing and hatching were created using 900 g/mol PCLTA at 50 wt% with 3 wt% photoinitiator. The scaffold dimensions were measured as described above and variability between sets at various slicing and hatching distances was reported as the standard error of the mean.

2.2.7 Scale-Up Optimization

Once the optimal printing parameters, concentration of monomer, concentration of photoinitiator and molecular weight were identified, a prototype of a graft to be used for sub-retinal transplantation in a small animal model was created. This circular scaffold had pore dimensions identical to those described above with an overall diameter of 1 mm and height of 0.1 mm. Samples were prepared, printed and processed as previously described, and images were collected using bright field, scanning electron, and confocal microscopy and analyzed as described above. Fluorescent images were collected using a Leica DM 2500 SPE confocal microscope (Leica Microsystems; Wetzlar, Germany).

2.2.8 *In vivo* Biocompatibility

Prior to transplantation, six two-photon polymerized PCL scaffolds were sterilized by submersion in 100% ethanol for 24 hours, followed by three 30-minute rinses with sterile 1xHBSS. All animal procedures were performed with permission of the University of Iowa IACUC and complied with the ARVO Statement for the Use of Animals in Ophthalmic and Vision Research (https://www.arvo.org/About/policies/statement-for-the-use-of-animals-in-ophthalmic-and-vision-research/). Four-month-old transgenic pigs carrying the human Pro23His mutation in the gene rhodopsin (RHO) were used as transplant recipients in order to model the ocular dimensions and sub-retinal conditions expected in human retinal degeneration.[29-30] Each of six animals (two males and four females) underwent sub-retinal transplantation of a 1 x 3 x 0.1 mm two-photon polymerized PCL scaffold (50 wt% PCLTA 900 created using 3 wt% photoinitiator) with vertical and horizontal pores as previously described. In the contralateral eye, four animals (two males and two females) received the same surgical treatment with no polymer and two animals (both female) received no treatment. Briefly, each animal subjected to surgery underwent a 23-gauge three-port vitrectomy for removal of the central vitreous and detachment of the posterior hyaloid. A sub-retinal bleb near the optic nerve and visual streak was raised with balanced salt solution on a 41-gauge needle as previously described.[31] An approximately 1.5 mm retinotomy was made within the bleb using endocautery and vertical scissors, and the scaffold was placed into the sub-retinal space with custom-built polymer forceps. The retina was subsequently flattened via a fluid-air exchange. The pigs received no systemic post-operative immune suppressive agents. Animals were sacrificed

by barbiturate overdose at one-month post-surgery, at which time indirect ophthalmoscopy and spectral-domain OCT (SD-OCT) were performed (Bioptigen Envisu R2200, Bioptogen, Inc., Morrisville, NC). Immediately post-ophthalmoscopic evaluation, eyes were enucleated and fixed in 4% paraformaldehyde overnight, then processed for morphologic analysis. Each animal subsequently underwent a complete necropsy to identify evidence of systemic toxicity and tumorigenicity. Retinal sections were assessed by using paraffin sections stained using hematoxylin and eosin (H&E) and immunohistochemistry and imaged using light and confocal microscopy, respectively. For immunohistochemistry, tissues were labeled with anti-recoverin antibody (Millipore, 1:250) to detect photoreceptor cells and DAPI for cell nuclei.

2.2.9 Statistical Analyses

Three-way analysis of variance

Three-way ANOVA was used to assess the relative contributions of three variables (polymer concentration, polymer molecular weight and slicing or hatching distance) on scaffold width and height as well as pore roundness and diameter. The limitations of the test required reducing the number of levels for each variable to two. For molecular weight, no more than two levels (300 g/mol and 900 g/mol) had been selected for the experiment, so all levels were included. For slicing and hatching, only the upper and lower bounds of the experimental range (0.1 μm and 0.5 μm) were selected for three-way ANOVA. Since the use of 900 g/mol PCLTA at 75 wt% resulted in poor or no printing and thus data could not be collected from this group, 25 wt% and 50 wt% were selected as the levels of interest for polymer concentration. Three-way ANOVA also demands an equal number of replicates for each sample, yet some scaffolds were

incomplete and did not have as many pores as designed. Thus, for pore diameter and roundness, we only included the first three measurements for each sample in our analysis. A few scaffolds were void of pores altogether, in which case zeros were used as the measurement of pore diameter and roundness. Data were assumed to be normally distributed and were assessed at a confidence interval of 95%. For each measured outcome, the percentage of variation attributed to each variable or interaction was reported as a pie chart.

Two-way analysis of variance

For each measured outcome, the two variables that contributed most to measurement variation (either alone or in interactions) were further analyzed via two-way ANOVA. For molecular weight, the levels were 300 g/mol and 900 g/mol. For slicing and hatching, levels were 0.1 μm, 0.5 μm, 1.0 μm and 1.5 μm. For polymer concentration, the experimental levels used for two-way ANOVA were 25 wt% and 50 wt% (as no data could be collected for 900 g/mol PCLTA at 75 wt%). Data were assumed to be normally distributed and were assessed at a confidence level of 95%. Where relevant, post-hoc Tukey's multiple comparisons tests were performed for slicing or hatching distance, while Sidak's multiple comparisons tests were performed for molecular weight and polymer concentration, each at a confidence level of 95%.

One-way analysis of variance

In the instance that polymer concentration was identified by three-way ANOVA as contributing strongly to variance, one-way ANOVA and Tukey's multiple comparisons tests were performed for 300 g/mol PCLTA only with 25 wt%, 50 wt%, and 75 wt% in addition to the two-way ANOVA described above that excluded 75 wt%. Data

were assumed to be normally distributed and were assessed at a confidence interval of 95%.

2.3 Results

2.3.1 Determination of Printing Thresholds

As expected, the laser power required to induce a two-photon polymerization event increased with increasing scanning speed (**Figure 2.1**). For both PCLDA and PCLTA, increasing molecular weight also slightly increased the laser power required for polymerization (**Figure 2.1A**). In fact, the largest molecular weight prepolymer we created for this study (PCLDA 2000) did not polymerize within the bounds of our experiment (at or above 6 mm/s with 100% laser power). However, for those PCLDA prepolymers that did polymerize, increasing molecular weight also increased the range of laser powers at which the structures resembled the model (**Figure 2.1B**). At all scanning speeds and regardless of molecular weight, polymerization of PCLDA required much higher laser power compared to PCLTA and simply did not polymerize at scanning speeds greater than 40 mm/s (**Figure 2.1A**). In addition, unlike PCLTA structures, most PCLDA structures did not resemble the modeled star or lacked intricate details such as star points (**Figure 2.1B**). Due to this poor polymerization, only the PCLTAs were considered for the remaining experiments.

.

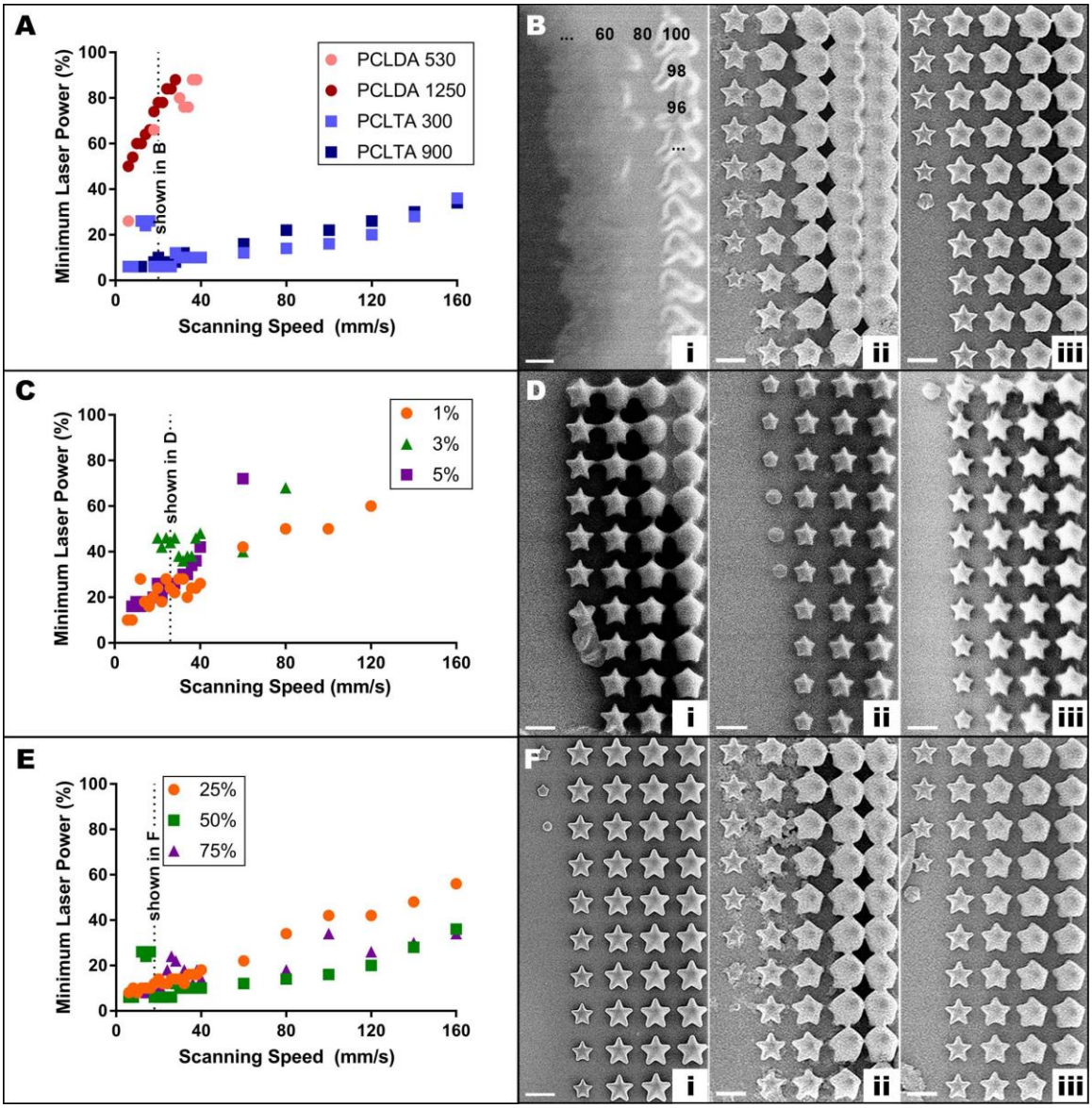

Figure 2.1. Two-photon polymerization threshold. **A**) Threshold profiles for four acrylated PCL prepolymers at fixed composition (50 wt% monomer, 3 wt% photoinitiator) with **B**) corresponding images of stars composed of crosslinked 1250 g/mol PCLDA (i), 300 g/mol PCLTA (ii) and 900 g/mol PCLTA (iii) fabricated at 20 mm/s. The numbers in sub-panel i indicate the laser power used at each star position. **C**) Threshold profiles for three photoinitiator concentrations in 50 wt% 900 g/mol PCLTA with **D**) corresponding images of stars of the same composition: 1 (i), 3 (ii) or 5 (iii) wt%

photoinitiator at 26 mm/s. **E**) Threshold profiles for three concentrations of 300 g/mol PCLTA with 3 wt% photoinitiator and **F**) corresponding images of stars of the same composition: 25 (i), 50 (ii) or 75 (iii) wt% prepolymer at 18 mm/s. Scale bars in B, D and F represent 10 μm.

Photoinitiator concentration did not cause clear differences in the minimum laser power required for polymerization (**Figure 2.1C**). However, qualitatively, crosslinked PCL structures formed with 1 wt% photoinitiator were larger and had fewer sharp edges than those formed with 3 or 5 wt% (**Figure 2.1D**). Thus, to conserve resources while maintaining optimal structure quality, 3 wt% was selected as the photoinitiator concentration for successive experiments.

At scanning speeds below 40 mm/s, the prepolymer concentration did not appear to affect polymerization threshold (**Figure 2.1E**). At scanning speeds above 40 mm/s, the 25 wt% formulations required higher laser power to polymerize than 50 wt% or 75 wt%. Although there were some scanning speeds at which 75 wt% PCLTA 300 required a higher laser power than 50 wt%, these differences were inconsistent across all scanning speeds. Furthermore, at a given scanning speed, the range of laser powers that resulted in structures that resembled the model was larger for 25 wt% PCLTA 300 than for 50 wt% or 75 wt% (**Figure 2.1F**). Similar results were noted for PCLTA 900 (data not shown). Taken together, these results indicated that polymer concentration may play a role in fidelity of structure to the model and that each formulation would require its own optimized scanning speed and laser power in order to achieve the best two-photon resolution.

2.3.2 Determination of Print Resolution

Regardless of polymer formulation, the use of high laser scanning speeds led to delamination of two-photon polymerized structures (**Figure 2.2A**). We aimed to avoid these aberrant features while also creating high-resolution tissue scaffolds within a feasible timeframe. Thus, we selected the fastest laser scanning speed that did not cause delamination (**Table 2.1**) and characterized resolution at that scanning speed to select optimal polymerization conditions. For each formulation, the star width at the polymerization threshold was smaller than the modeled width (**Figure 2.2B-C**). This width increased with increasing laser power, except in the case of 75 wt% PCLTA 900, which at the selected scanning speed produced stars smaller than the modeled star regardless of laser power (**Figure 2.2C**). 50 wt% and 75 wt% PCLTA 300 were characterized at the same scanning speed (40 mm/s), as were 25 wt% and 50 wt% PCLTA 900 (60 mm/s). Thus, these resolution trends can be compared directly to infer the influence of polymer concentration on feature width. For PCLTA 300, increasing the polymer concentration increased the laser power necessary to achieve star widths similar to the modeled width, while the overall width per laser power ratio (slope) appeared to be independent of polymer concentration (**Figure 2.2B**). Conversely, the width of structures created with 25 wt% or 50 wt% PCLTA 900 did not appear to be influenced by polymer concentration (**Figure 2.2C**). For each formulation, the laser power that resulted in a mean point-to-point distance closest to the design (~9.5 μm) was chosen as the optimal laser power for future two-photon polymerization experiments (**Table 2.1**).

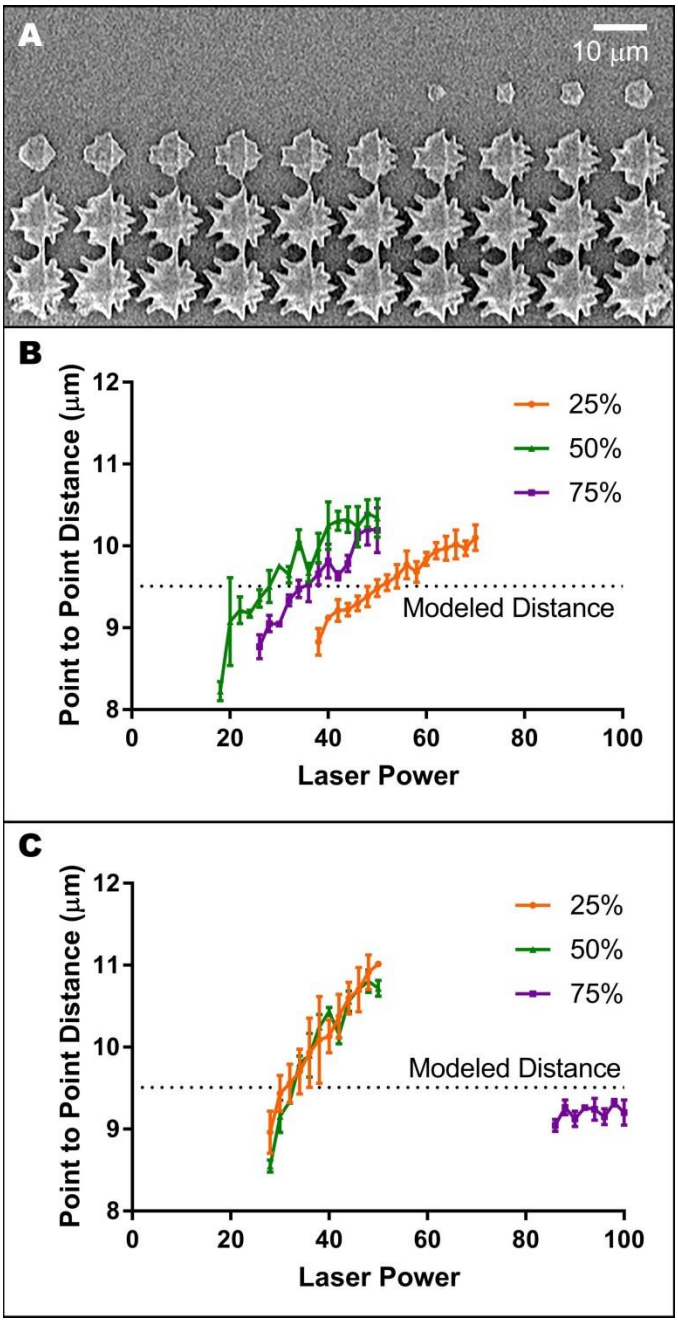

Figure 2.2: Determining optimal laser power and scanning speed. **A**) Representative image of undesirable, delaminated two-photon polymerized structures. **B-C)** Width of stars created using the fastest scanning speed that did not result in delamination for 300 g/mol (**B**) and 900 g/mol (**C**) PCLTA at three prepolymer concentrations, each with 3

wt% photoinitiator. Each point represents the mean (n=3), while error bars represent the standard deviation and the dotted line represents modeled star point-to-point distance.

Table 2.1: Optimal scanning speeds and laser powers for PCLTA formulations with 3 wt% photoinitiator.

Molecular Weight (g/mol)	[Polymer] (wt%)	Scanning Speed (mm/s)	Laser Power (%)
300	25	36	50
	50	40	28
	75	40	36
900	25	60	32
	50	60	32
	75	18	100

2.3.3 Analysis of Model to Scaffold Fidelity

Scaffold Width

With a constant hatching distance, the variables slicing distance and molecular weight, as well as their interactions with each other and with prepolymer concentration, were statistically significant ($p < 0.0001$) contributors to variability in scaffold width (**Table 2.S1A**). Prepolymer concentration alone was the only non-significant variable ($p = 0.8493$). Specifically, the variables that contributed most to the width of structures were molecular weight and slicing distance, which caused 33% and 34% of the total variation,

respectively (**Figure 2.3A**). Narrowing the analysis using the average across all polymer concentrations reinforced the significance of slicing distance and molecular weight ($p < 0.0001$) rather than their interaction (**Table 2.S1B**). In general, increasing slicing distance or increasing molecular weight decreased scaffold width, meaning that the structures were more dissimilar to the model (**Figure 2.3A-B**). Regardless of molecular weight, using a slicing distance of 1.0 or 1.5 μm resulted in scaffolds with significantly smaller widths ($p < 0.05$) than scaffolds created using a slicing distance of 0.1 μm (**Table 2.S1C**). Furthermore, the difference in scaffold width between 300 and 900 g/mol was significant ($p < 0.05$) for all slicing distances except 0.5 μm (**Table 2.S1D**).

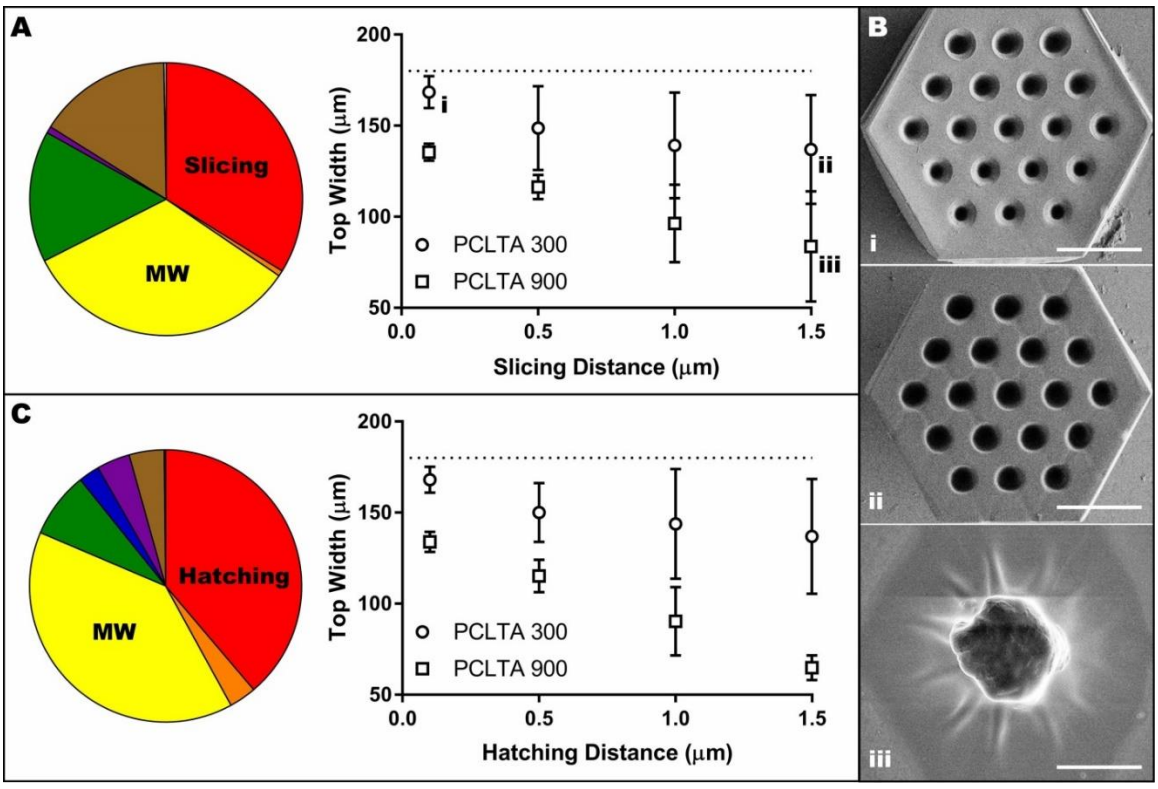

Figure 2.3: Influence of slicing distance, hatching distance and molecular weight on scaffold width. **A)** Pie chart representing the contribution of experimental variables on scaffold width with constant hatching of 0.5 μm and a consolidated graphical analysis

showing only the effect of slicing distance and molecular weight (data points were averaged across all polymer concentrations). Lower case Roman numerals are a cross-reference to Panel B. **B**) Representative images of the effect of slicing distance and molecular weight on the width of PCL scaffolds: 300 g/mol with 0.1 μm slicing distance (i), 300 g/mol with 1.5 μm slicing distance (ii), and 900 g/mol with 1.5 μm slicing distance with all other variables held at 75 wt% prepolymer and 0.5 μm hatching distance. Scale bars represent 50 μm. **C)** Pie chart representing the contribution of experimental variables on scaffold width with constant slicing of 0.5 μm and a consolidated graphical analysis showing only the effect of hatching distance and molecular weight (data points were averaged across all polymer concentrations). In **A** and **C**, the dotted line indicates the designed width of 180 μm and the colors represent the following variables: red, slicing or hatching distance; orange, interaction between slicing or hatching distance and molecular weight; yellow, molecular weight; green, interaction between molecular weight and prepolymer concentration; blue, prepolymer concentration; purple, interaction between prepolymer concentration and slicing or hatching distance; brown, interaction between slicing or hatching distance, molecular weight and prepolymer concentration; grey, other.

When slicing distance was held constant, trends in scaffold width were similar to those observed when hatching distance was constant. Although all variables and their interactions played significant roles in scaffold width ($p < 0.0001$, **Table 2.S1E**), the greatest contributors to variation were hatching distance (39%) and molecular weight (39%) (**Figure 2.3C**). In a subsequent consolidated analysis examining only hatching

distance and molecular weight, both factors and their interaction were significant ($p < 0.05$). However, the factors contributed more independently to the variation than their interaction (26% and 44% for hatching distance and molecular weight, respectively, compared to 5% for their interaction) (**Table 2.S1F**). In general, increasing hatching distance or molecular weight decreased scaffold width (**Figure 2.3C**), thus causing a decrease in the extent to which the scaffold resembled the model. For a molecular weight of 300 g/mol, the only significant difference in scaffold width was between 0.1 and 1.5 μm ($p < 0.01$). The effect of hatching distance was more pronounced for 900 g/mol: using a hatching distance of 0.1 μm resulted in significantly wider scaffolds than using a hatching distance of 1.0 or 1.5 μm ($p < 0.01$, **Table 2.S1G**). Furthermore, using a hatching distance of 0.5 μm resulted in a significantly larger scaffold width than the use of 1.5 μm ($p < 0.001$, **Table 2.S1G**). Conversely, the use of 300 g/mol PCLTA resulted in significantly wider scaffolds than 900 g/mol PCLTA at every hatching distance ($p < 0.01$, **Table 2.S1H**).

When slicing distance was held constant, trends in scaffold width were similar to those observed when hatching distance was constant. Although all variables and their interactions played significant roles in scaffold width ($p < 0.0001$, **Table 2.S1E**), the greatest contributors to variation were hatching distance (39%) and molecular weight (39%) (**Figure 2.3C**). In a subsequent consolidated analysis examining only hatching distance and molecular weight, both factors and their interaction were significant ($p < 0.05$). However, the independent factors contributed more to the variation than the interaction (26% and 44% for hatching distance and molecular weight, respectively, compared to 5% for their interaction) (**Table 2.S1F**). In general, increasing hatching

distance or molecular weight decreased scaffold width (**Figure 2.3C**), thus causing a decrease in the extent to which the scaffold resembled the model. For a molecular weight of 300 g/mol, the only significant difference in scaffold width was between 0.1 and 1.5 μm ($p < 0.01$). The effect of hatching distance was more pronounced for 900 g/mol: using a hatching distance of 0.1 μm resulted in significantly wider scaffolds than using a hatching distance of 1.0 or 1.5 μm ($p < 0.01$, **Table 2.S1G**). Furthermore, using a hatching distance of 0.5 μm resulted in a significantly larger scaffold width than the use of 1.5 μm ($p < 0.001$, **Table 2.S1G**). Conversely, the use of 300 g/mol PCLTA resulted in significantly wider scaffolds than 900 g/mol PCLTA at every hatching distance ($p < 0.01$, **Table 2.S1H**).

Vertical Pore Diameter

At a constant hatching distance, the interaction between molecular weight and concentration of prepolymer had the largest effect of the experimental variables on scaffold vertical pore diameter, contributing 62% of the total variation (**Figure 2.4A-B** and **Table 2.S2A-B**). At 25 wt% polymer, the pores of scaffolds created using 300 g/mol PCLTA were significantly larger (i.e., closer to the modeled diameter) than the pores of scaffolds created using 900 g/mol PCLTA, while at 50 wt% the 900 g/mol pores were larger than their low molecular weight counterparts ($p < 0.0001$, **Table 2.S2C**). In fact, the pore size of 900 g/mol PCLTA scaffolds increased significantly when prepolymer concentration increased from 25 to 50 wt% ($p < 0.0001$, **Table 2.S2D**). Conversely, the diameter of 300 g/mol PCLTA scaffold pores decreased significantly as concentration increased from 25 to 50 wt%, then increased again when the concentration was further increased to 75 wt% (both $p < 0.0001$, **Table 2.S2D-E**). The 75 wt% 900 g/mol PCLTA

consistently over-polymerized, filling the pores and solidifying all printed structures into a block (data not shown).

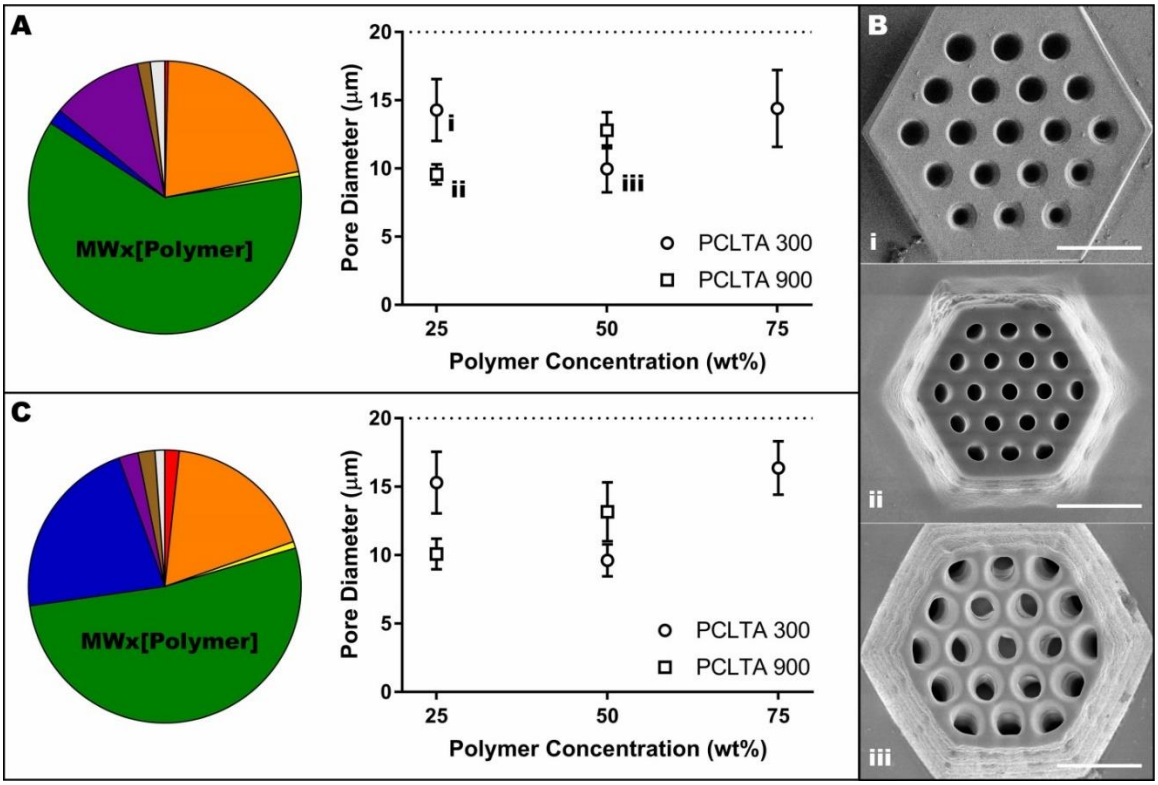

Figure 2.4: Influence of molecular weight and prepolymer concentration on the vertical pore diameter of PCLTA scaffolds. **A)** Pie chart representing the contribution of experimental variables on pore diameter with constant hatching distance of 0.5 μm and a consolidated graphical analysis showing only the effect of molecular weight and prepolymer concentration (data points were averaged across all hatching distances). Lower case Roman numerals are a cross-reference to Panel B. **B**) Representative images of the effect of molecular weight and prepolymer concentration on pore diameter: 25 wt% 300 g/mol (i), 25 wt% 900 g/mol (ii) and 50 wt% 300 g/mol (iii) with all other variables held at 1.5 μm slicing distance and 0.5 μm hatching distance. Scale bars represent 50 μm. **C)** Pie chart representing the contribution of experimental variables on

pore diameter with constant slicing distance of 0.5 μm and a consolidated graphical analysis showing only the effect of molecular weight and prepolymer concentration (data points were averaged across all slicing distances). In **A** and **C**, the dotted line indicates the designed pore diameter of 20 μm and the colors represent the following variables: red, slicing or hatching distance; orange, interaction between slicing or hatching distance and molecular weight; yellow, molecular weight; green, interaction between molecular weight and prepolymer concentration; blue, prepolymer concentration; purple, interaction between prepolymer concentration and slicing or hatching distance; brown, interaction between slicing or hatching distance, molecular weight and prepolymer concentration; grey, other.

Similarly, at constant slicing distance, the interaction between molecular weight and prepolymer concentration contributed the most to variations in scaffold vertical pore diameter (52% of total, **Figure 2.4C** and **Table 2.S2F-G**). As in the constant hatching experiment, increasing molecular weight decreased pore diameter at 25 wt% but increased pore diameter at 50 wt% (both $p < 0.0001$, **Table 2.S2H**). Likewise, increasing polymer concentration from 25 to 50 wt% increased pore diameter for 900 g/mol PCLTA ($p < 0.0001$, **Table 2.S2I**). On the other hand, for 300 g/mol PCLTA, scaffold pore diameter decreased as polymer concentration increased from 25 to 50 wt%, but increased again between 50 and 75 wt% ($p < 0.0001$, **Table 2.S2I-J**). Consistent with the hatching experiments, the 75 wt% 900 g/mol PCLTA over-polymerized and thus was omitted from these results.

Scaffold Height

Overall, slicing distance (55% of variation) and, to a lesser extent, molecular weight (12% of variation) dictated scaffold height at a constant hatching distance (**Figure 2.S4A-B** and **Table 2.S3A-B**). In general, scaffold height decreased with increasing slicing distance or molecular weight. Specifically, 300 g/mol PCLTA scaffolds created using a slicing distance of 1.5 μm were significantly shorter than those created using a slicing distance of 0.1 or 0.5 μm (both $p < 0.05$, **Table 2.S3C**). This effect was even more pronounced in 900 g/mol samples: scaffolds created using a slicing distance of 1.5 μm were significantly shorter than those created with slicing distances of 0.1, 0.5, or 1.0 μm ($p < 0.0001$, $p < 0.0001$ and $p < 0.001$, respectively, **Table 2.S3C**). Meanwhile, scaffolds created using 900 g/mol PCLTA were only significantly shorter than those composed of 300 g/mol PCLTA at a slicing distance of 1.5 μm ($p < 0.0001$, **Table 2.S3D**).

When slicing distance was held constant, prepolymer concentration contributed the most to variations in scaffold height (45%) followed by an interaction between all of the factors (16%, **Figure 2.S4C, Table 2.S3E**). When scaffold heights were averaged across both molecular weights (**Table 2.S3F**), overall their values decreased with increasing hatching distance and were maximal at a prepolymer concentration of 50 wt%. In fact, 50 wt% and 75 wt% scaffolds were significantly taller when created using a hatching distance of 0.1 μm compared to 1.0 or 1.5 μm hatching distances ($p < 0.05$ and $p < 0.01$, respectively, **Table 2.S3G**). Differences in the height of scaffolds created using 25 wt% versus 75 wt% prepolymer were not significant at any hatching distance (**Table 2.S3H**). Conversely, the use of 50 wt% prepolymer resulted in significantly taller

scaffolds than those composed of either 25 wt% or 75 wt% at each hatching distance (**Table 2.S3H**).

Vertical Pore Roundness

The two largest contributing factors to vertical pore roundness at constant hatching distance were the interaction between molecular weight and prepolymer concentration (38%) and the interaction between slicing distance and prepolymer concentration (21%, **Figure 2.S5A-B** and **Table 2.S4A**). It should be noted that in this instance, averaging across all slicing distances and removing 75 wt% from the analysis (due to incomplete data), inflated the influence of polymer concentration and de-emphasized the importance of the interaction between molecular weight and prepolymer concentration (**Table 2.S4B**). Nonetheless, under these circumstances, pores were significantly more round when scaffolds were created using 300 g/mol versus 900 g/mol PCLTA at 25 wt%, but the opposite occurred at 50 wt% ($p < 0.001$ and $p < 0.05$, respectively, **Table 2.S4C**). For either molecular weight, pore roundness significantly decreased when prepolymer concentration increased from 25 wt% to 50 wt% (both $p < 0.0001$, **Table 2.S4D**), but increasing the prepolymer concentration from 50 to 75 wt% (data only available for 300 g/mol PCLTA) resulted in a subsequent increase in pore roundness, though this value was still significantly smaller than the roundness at 25 wt% (all $p < 0.0001$, **Table 2.S4E**).

Prepolymer concentration had the greatest impact on pore roundness at a constant slicing distance (42% of variation), followed by the interaction between all of the variables (15%, **Figure 2.S5C** and **Table 2.S4F-G**). Increasing molecular weight significantly decreased pore roundness ($p < 0.0001$), but only with the use of 25 wt%

prepolymer (**Table 2.S4H**). Furthermore, similar to the results described above for constant hatching distance, pore roundness significantly decreased when prepolymer concentration increased from 25 wt% to 50 wt% (both $p < 0.0001$, **Table 2.S4I**), but increasing the prepolymer concentration from 50 wt% to 75 wt% resulted in a subsequent increase in pore roundness, though this value was still significantly smaller than the roundness at 25 wt% (all $p < 0.0001$, **Table 2.S4J**).

Horizontal Pore Quality

At a constant hatching distance, horizontal pore quality depended most on prepolymer concentration (mean difference of 1.25 versus 0.75 for either slicing distance or molecular weight, **Table 2.S5A**). Overall, maximal pore quality occurred in samples created using a prepolymer concentration of 50 wt% (**Figure 2.S6A-B**). Increasing molecular weight qualitatively increased horizontal pore integrity, while the effect of increasing slicing distance was less distinct (**Figure 2.S6A-B**). Similarly, prepolymer concentration contributed the most to horizontal pore quality (46%) at a constant slicing distance (**Table 2.S5B**). As in the experiment where hatching distance was held constant, in general maximal pore quality was achieved through the use of 50 wt% 900 g/mol PCLTA (**Figure 2.S6C**).

Reproducibility

At a constant formulation (i.e. prepolymer concentration and molecular weight) and hatching distance, increasing the slicing distance did not noticeably reduce the deviance of vertical pore diameter or roundness from the design values (**Figure 2.S7A**). Conversely, scaffold width became more variable as slicing distance increased, while scaffold height deviance initially decreased, then sharply increased with increasing

slicing distance (**Figure 2.S7A**). The variability of scaffold features due to hatching distance was overall smaller than the variability caused by varying slicing distance (**Figure 2.S7B**). In fact, all standard errors of the mean appeared to be independent of hatching distance and were less than 10%, except for the variability of scaffold width at a hatching distance of 1.5 μm.

2.3.4 Scale-Up Optimization

To feasibly treat an area of tissue with scaffold-assisted cell therapy, an implant with tissue-relevant overall dimensions is necessary. Specifically, as patients who retain even just the central 1mm of their retina may have very useful vision, the goal was to be able to print scaffolds that are a minimum of 1mm in diameter, preferably larger. Fabrication of a continuous two-photon polymerized structure using the instrument we describe here is limited to an area roughly 250 μm x 250 μm in size. Structures larger than this may be constructed as a series of segments that are "stitched" together by slightly overlapping the laser path and thus covalently linking each segment to its neighbors. Thus, the effect of the described variables on scaffold width determined, to some extent, their contributions to scale-up success or failure. For example, we initially selected formulation variables that were expected to result in scaffolds with maximal width and acceptable height and vertical pore dimensions (75 wt% 300 g/mol PCLTA), but chose the highest slicing and hatching distances (each 1.5 μm) in order to minimize fabrication time of a 1 mm diameter scaffold. Although the resulting scaled-up scaffold took only one hour to create, it lacked essential structural integrity in the stitches between segments (**Figure 2.5A**) and did not withstand even gentle handling. Decreasing both slicing and hatching distance to 1.0 μm increased the fabrication time to seven hours,

while significantly improving structural integrity (**Figure 2.5B**) and mechanical robustness.

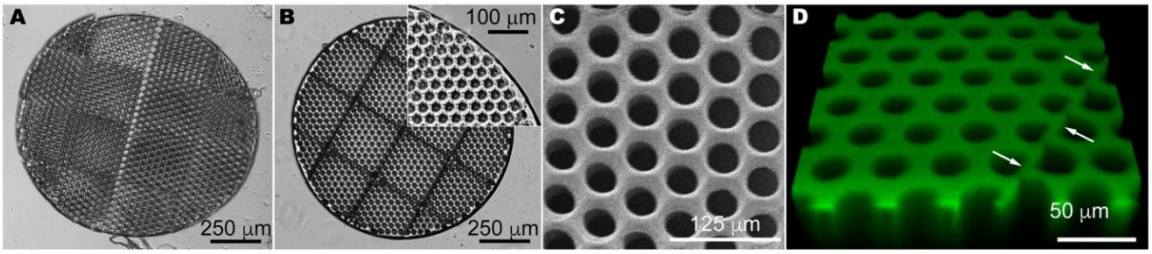

Figure 2.5: Scale-up of optimized two-photon polymerization to transplantation-relevant size. Light micrographs of scaffolds created using 75 wt% 300g/mol PCLTA with slicing and hatching distances of either 1.5 µm (**A**) or 1.0 µm (**B**). Further imaging of the 1.0 µm slicing and hatching sample previously described, using SEM (**C**) and confocal microscopy (**D**, polymer autofluorescent when excited with 488 nm laser).

Higher magnification methods, namely SEM and Confocal microscopy, were pursued to validate structural accuracy and fidelity of the scaled up scaffold. As shown in **Figure 2.5C and D**, the scaffold to model fidelity, as indicated by adherence of the vertical pores to the original model, was maintained. Specifically, the diameter and roundness of the vertical pores in this scaled-up scaffold are 15.9 ± 4.07 µm and 0.866 ±0.0889, respectively, which is consistent with the preliminary, single print area scaffold outcomes. Likewise, pores were free of excess polymer and the stitching edges remained intact (i.e. **Figure 2.5D** arrows, flat surface between vertical pores created during the stitching process, which is essential for structural integrity of the scaled-up scaffold),

indicating that this scaled-up scaffold was structurally conserved during post-fabrication processing.

2.3.5 *In vivo* Biocompatibility

The desired purpose of this work is to not only fabricate a highly intricate and degradable tissue scaffold at human-relevant size scales, but also to demonstrate the biocompatibility of such material. For this analysis, rectangular scaffolds were designed with the same porous structure as the generic scaffolds described above and printed at the maximum size (1 x 3 x 0.1 mm) that could be readily placed beneath the retina surgically using custom-developed instrumentation. One month after transplantion of these scaffolds into the sub-retinal space of retinal degenerative Pro23His rhodopsin transgenic pigs (i.e., a model of autosomal dominant retinitis pigmentosa),[29] no evidence of uveitis (i.e., intraocular inflammation) was detected on ophthalmoscopic examination. Using optical coherence tomography, the scaffolds were imaged and observed to be lying flat in the correct location within the sub-retinal space (**Figure 2.6A-B**). Post-mortem histological observation demonstrated that host photoreceptor and retinal pigment epithelial cells had migrated into the scaffold further implying that the scaffold was well tolerated and biocompatible (**Figure 2.6C-F**). In addition, recoverin-labeled photoreceptor cells were maintained both above and inside the vertical pores of the auto-fluorescent PCLTA scaffold (**Figure 2.6E-F**). In addition, no evidence of toxicity to adjacent photoreceptor cell and/or inner retinal neurons was detected (**Figure 2.6C-F**). Finally, following gross necropsy, there was no evidence of tumor formation or tissue necrosis to suggest abnormal cellular proliferation or systemic toxicity in any of the tissues listed in **Table 2.S6**.

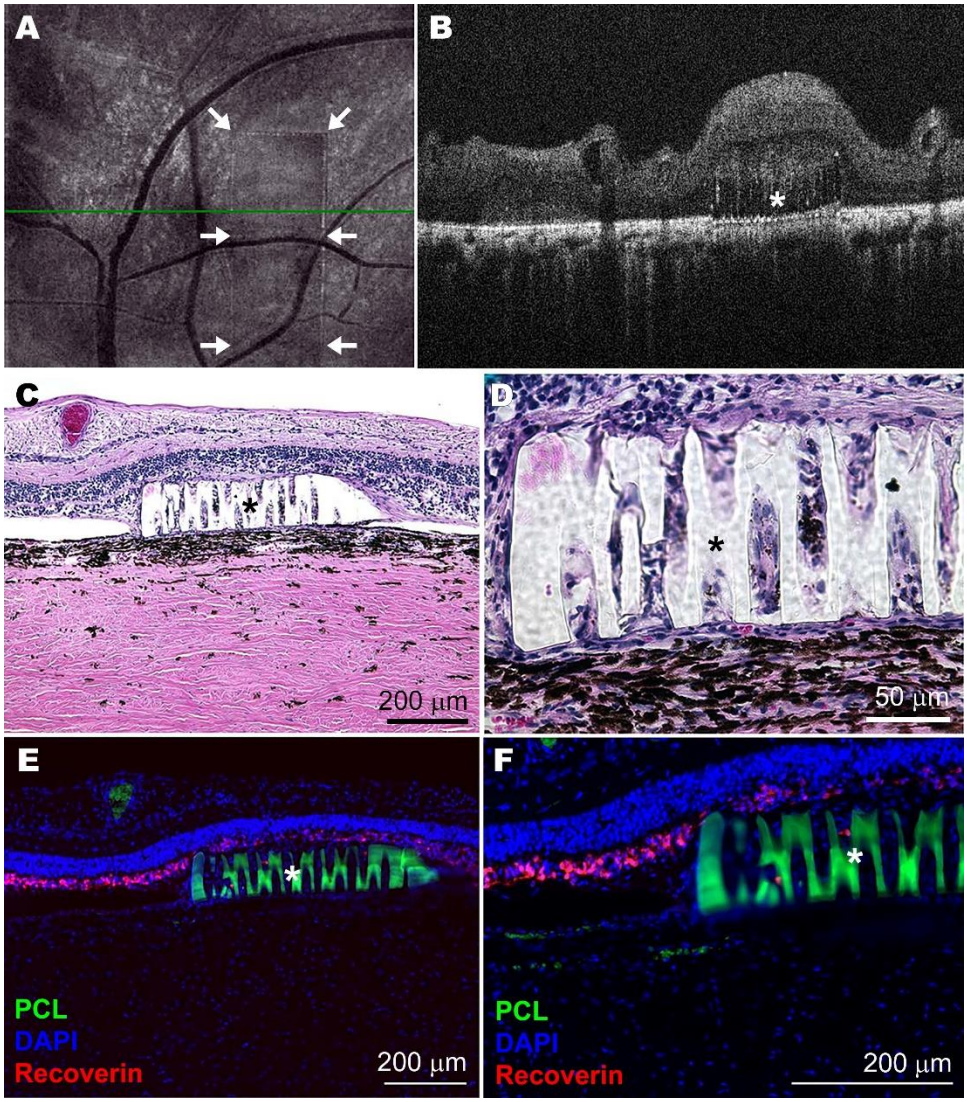

Figure 2.6: Scaled-up prototype of crosslinked PCLTA 900 in the degenerating pig sub-retinal space 30 days after transplantation. Representative *en face* (**A**) and horizontal B-scan (**B**) optical coherence tomographs (green line in A indicates cross-sectional plane shown in B) of the post-mortem Pro23His pig eye show placement of the transplanted polymer (border indicated with arrows in A and marked with * in B). Representative histological (**C-D**) and immunohistochemical (**E-F**) images of retinal sections show the embedded PCL scaffolds (marked with * and in E-F also autofluorescent in green) and surrounding tissue.

2.4 Discussion

Scientific and commercial interest in two-photon lithography has steadily grown since its inception more than twenty years ago. To date, however, its use for studying or treating human disease has been limited by the unavailability of suitable technologically and biologically compatible prepolymers. Poly(caprolactone), a component of several FDA-approved devices, is well-characterized in the literature, and its physical properties can be easily manipulated. In this study, we used photo-curable multi-acrylated PCL to demonstrate how biologically relevant polymers in general can be optimized for use in two-photon polymerization systems. Through extensive testing to define optimal printing parameters, we further demonstrate that two-photon polymerization as a method of creating high-quality 3D structures depends on several factors, including prepolymer functionality, molecular weight, and concentration.

Because of the greater concentration of reactive groups, we expect that prepolymers with high functionalities and low molecular weights will form more highly cross-linked structures upon polymerization than their low functionality and high molecular weight counterparts. Our results support the concept that the faster polymerization rate from greater reactive group concentration also leads to a high degree of structure retention and fidelity to the model. For example, in general, PCLTA required less laser exposure to undergo two-photon polymerization than PCLDA (**Figure 2.1**). Furthermore, integrity to the model was conserved during two-photon polymerization of PCLTA, but not of PCLDA. Although the differences were slight, increasing molecular weight also increased the laser exposure needed to achieve a two-photon polymerization event. In fact, the highest molecular weight prepolymer we studied (PCLDA 2000) did

not polymerize at even the slowest scanning speeds and highest intensity laser exposures. The effect of molecular weight also extended to larger structures; decreasing molecular weight increased scaffold width (**Figure 2.3**) and vertical pore diameter (**Figure 2.4**), each of which represent improved accuracy to the model.

The extent to which two-photon polymerized scaffolds match the 3D model is important not only for reliability and reproducibility of a material, but also for proper function and scale-up. Based on our preliminary studies, we hypothesized that minimizing structure shrinkage was critical to achieving successful scale-up. Creating larger, translationally relevant scaffolds requires "stitching" of smaller segments. If the width of each segment is too small, these pieces will not form proper connections with one another. Thus, according to our measurements of scaffold width, we selected 300 g/mol PCLTA for our scale-up studies, as it produced structures that were closer to the 3D design than 900 g/mol PCLTA (**Figure 2.3**). Vertical pores, designed to hold stem cell derived photoreceptor cells in a pseudostratified epithelium as in the retinal outer nuclear layer, are the most important functional feature of our proposed scaffolds. Although the dimensions of the pores can easily be tuned by adjusting the 3D model, adherence to the model without a need for retrospective adjustment is strongly preferred. Thus, we chose to use a prepolymer concentration of 75 wt%, which resulted in the least amount of pore shrinkage (**Figure 2.4**). Although our data also indicated that the use of small slicing and hatching distances would result in the least deviant structures, fabrication time is a major concern for the adoption and scale-up of two-photon polymerization in biotechnology. We were able to balance these two factors during scale-

up by selecting slicing and hatching distances that resulted in larger scaffolds with excellent integrity and reasonable production time (**Figure 2.5**).

A common concern for tissue scaffolds is matching the physical properties of a material to the native tissue. While in this study we show that increasing molecular weight presents a number of disadvantages with regard to two-photon polymerization, decades of literature show that increasing molecular weight between cross-links decreases elastic modulus. This adjustment would theoretically cause materials to better match the mechanical properties of human tissue. An estimate of the apparent modulus of each scaffold generated in this study can be calculated from the known moduli of bulk PCLTA. In a separate study (manuscript in preparation), we report the bulk elastic moduli of PCLTA 300 and 900 g/mol to be 6.93 MPa and 3.97 MPa, respectively. However, introducing the intricate structure we describe here will certainly change the modulus of the overall material. To estimate this change, we use the equation for a longitudinally-loaded fibrous composite:

$$E_C = E_M V_M + E_f V_f \quad \textbf{(1)}$$

where E and V are elastic modulus and volume fraction, respectively, and subscripts C, M, and F refer to composite, matrix, and fiber. To apply this equation to this study, we assume that the vertical pores are fibers of fluid in a matrix of PCLTA and that the horizontal pores do not contribute to the compressive modulus because they are not engaged in compressive force loading. Accordingly, the estimated apparent moduli of scaffolds created in this study are 2.56 MPa and 1.47 MPa for PCLTA 300 and 900 g/mol, respectively. In each case, the modulus is still far greater than that of the native tissue.[32] Copolymerization of PCL with a biocompatible plasticizer could lower the

modulus, enabling better mechanical matching with human tissues. Furthermore, the same technique described here could potentially be applied to a wide variety of soft biomaterials, such as PEG or chitosan hydrogels.

We have previously shown that two-photon polymerization can be used to create scaffolds using commercially available, non-degradable photoresists that encourage vertical orientation of retinal progenitor cells.[28] In this study, we have presented promising results to suggest that two photon polymerized PCL based photoreceptor cell delivery scaffolds are compatible with the degenerative host retina (**Figure 2.6**). Specifically, at 1-month following subretinal transplantation of scaled photoreceptor cell delivery scaffolds in the non-immune suppressed Pro23His rhodopsin mutant retinal degeneration pig, no sign of scaffold-inflicted retinal injury, inflammation, systemic toxicity, or tumor formation was detected. The fact that the Pro23His rhodopsin pig has a retinal degenerative disease akin to patients with retinitis pigmentosa and that its eye is anatomically similar to human, supports the translatability of the reported surgical approach and scaffold for human cell replacement strategies. Moreover, as the method we present can be adapted to a wide range of polymer chemistries, our results can be utilized for a variety of different biomedical applications beyond retinal cell replacement. Given that microstructural control of degradable polymers has historically been a limitation for many applications, this work represents a significant step forward in the field of precision biomaterials.

2.5 Supplemental Information

2.5.1 Supplemental Materials and Methods

Calculation of Scaffold Height

Most scaffolds shrunk to a greater degree on top than on bottom, thus taking the general form of a truncated hexagonal pyramid (**Figure 2. S2A**) of unknown height (h) and with faces that lie at a constant but unknown angle to the horizontal plane (θ).We imaged each scaffold from directly above (**Figure 2. S2B**) and collected triplicate measurements of the width at the top of the scaffold (W_t) and a single measurement of the width at the bottom of the scaffold (W_b). Using these values, we calculated the difference in top and bottom widths (ΔW) and the horizontal distance between the top and bottom edges of the scaffold (a), as follows.

$$\Delta W = W_b - W_{t,avg} \quad \textbf{(S1)}$$

$$\mathrm{d} = \frac{\Delta \mathrm{W}}{2} \sin(60°) \quad \textbf{(S2)}$$

To better understand the vertical features, we also imaged each scaffold at a 30° tilt (**Fig. S1C**), measuring the projected horizontal distance between the top and bottom edge at the front of the scaffold (d_p) in triplicate. These measurements were merely 2D projections of 3D features (**Fig. S1D**), so we used the measured values to construct trigonometric relationships to solve for the unknown scaffold height. For example, visualizing the scaffold, measured values, and desired value from the left facilitates the creation of two useful triangles (**Figure 2.S1E**). A series of equations based on these triangles was used to solve for the scaffold height. First,

$$\sin(120° - \theta) = \frac{d_{p,avg}}{x} \quad \textbf{(S3)}$$

Using a trigonometric identity to substitute yields:

$$\sin(120°)\cos(\theta) - \cos(120°)\sin(\theta) = \frac{d_{p,avg}}{x} \quad \textbf{(S4)}$$

Based on the second triangle,

$$\cos(\theta) = \frac{d}{x} \quad \textbf{(S5)}$$

$$\sin(\theta) = \frac{h}{x} \quad \textbf{(S6)}$$

Therefore,

$$\frac{d}{x}\sin(120°) - \frac{h}{x}\cos(120°) = \frac{d_{p,avg}}{x} \quad \textbf{(S7)}$$

$$h = 2\left(d_{p,avg} - 0.866d\right) \quad \textbf{(S8)}$$

2.5.2 Figures

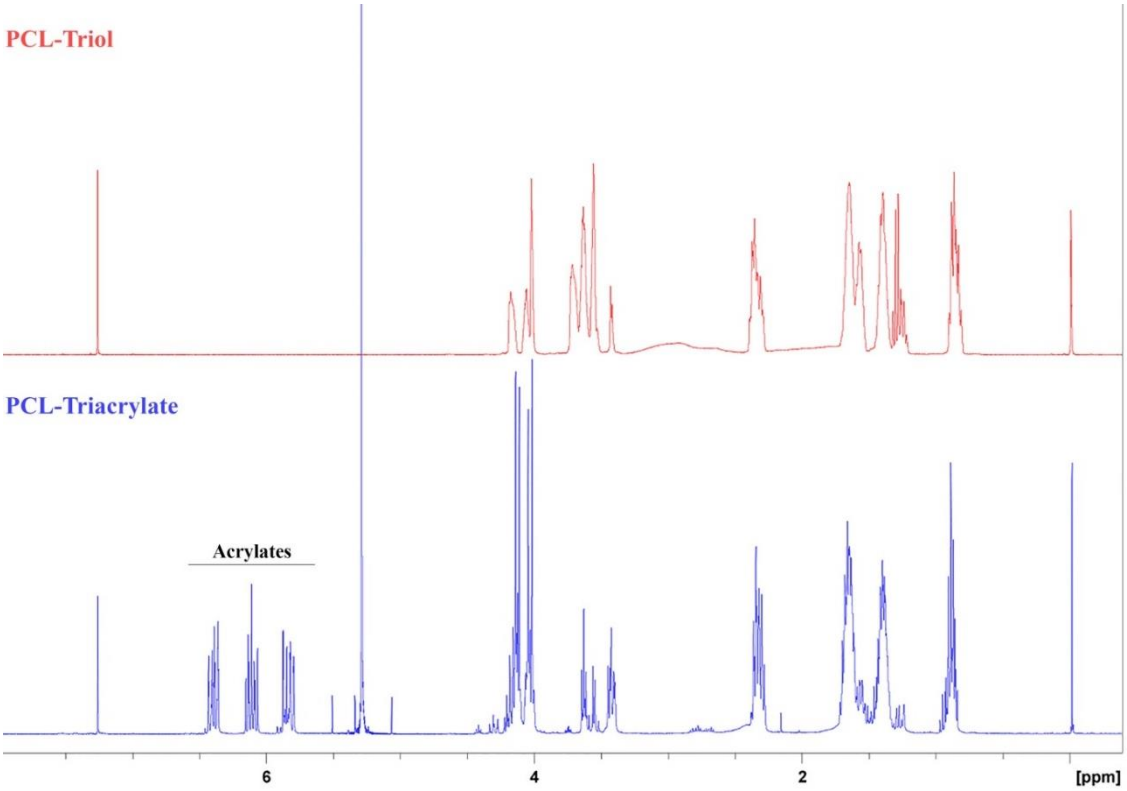

Figure 2.S1: Representative Validation of Acrylation with Nuclear Magnetic Resonance Imaging. NMR spectrum of PCL-triol (red) and PCL-triacrylate (blue). Evidence of successful acrylation can be evaluated by the triplet of multiplets from 5.75-6.5 ppm. Residual dichloromethane created an intense peak at 5.25 ppm.

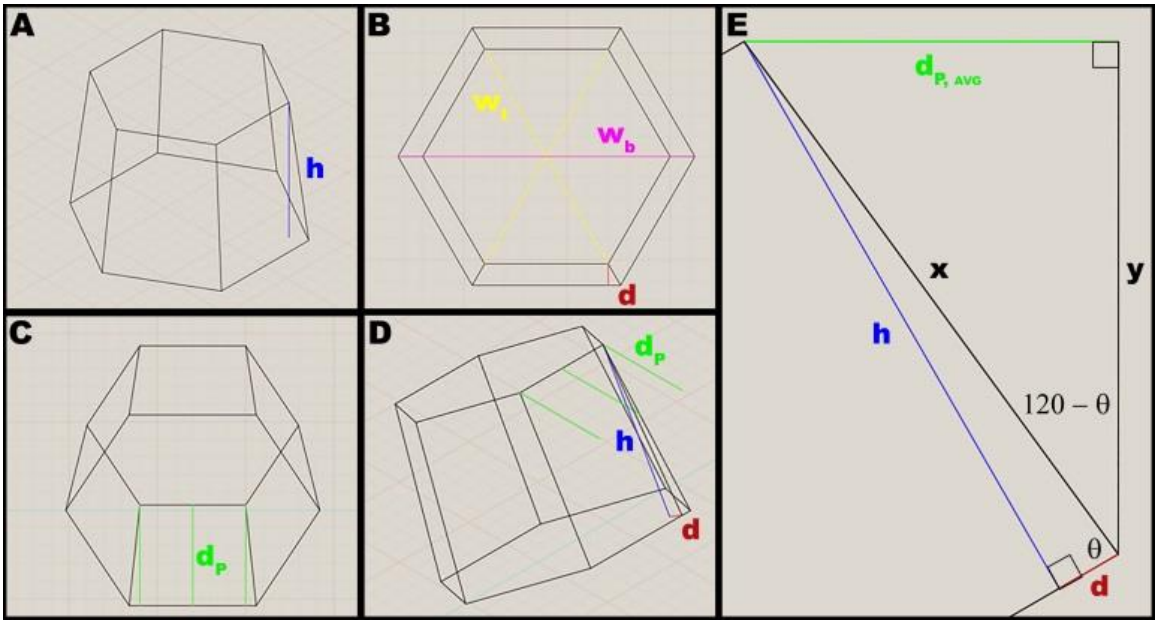

Figure 2.S2: Schematic of process used to calculate the height of truncated hexagonal pyramid scaffolds. **A)** Isometric southwest, wireframe view of a scaffold of unknown height (h, blue). **B)** Top view showing three measurements of the top width (W_t, yellow), one measurement of the bottom width (W_b, magenta), and the calculated horizontal distance between top and bottom edges (d, red). **C)** Top view of a scaffold that has been tilted back 30° showing three measurements of horizontal distance between top and bottom edge (d_p, green). **D)** Isometric southwest view of tilted scaffold with unknown height (h, blue) showing the calculated horizontal distance between top and bottom edges (d, red) and the horizontal distance between top and bottom edges, as projected when viewed from above (d_p, green). **E)** 2D Trigonometric relationships used to calculate scaffold height.

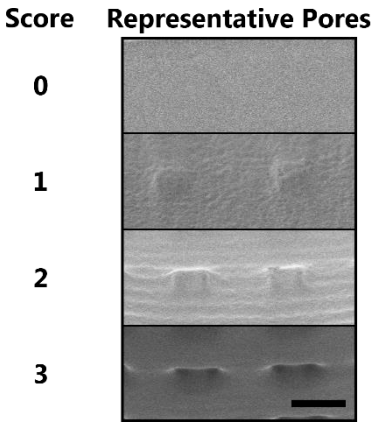

Figure 2.S3: Pore quality scale used to compare horizontal pores. The quantitative scale used to rate and describe the horizontal pore quality. The scale bar represents 10 μm.

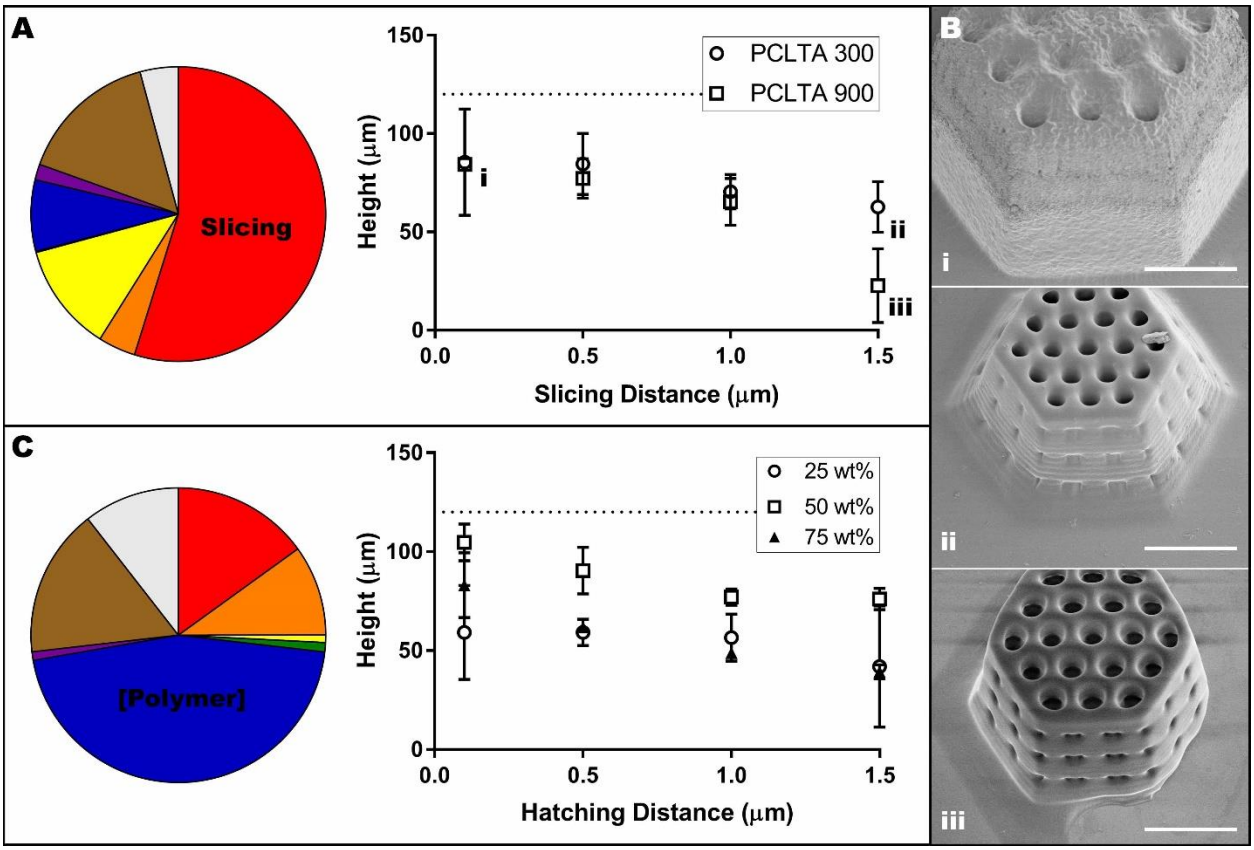

Figure 2.S4: Influence of slicing distance, hatching distance and molecular weight on scaffold height. **A)** Pie chart representing the contribution of experimental variables on pore diameter with constant hatching distance of 0.5 μm and a consolidated graphical analysis showing only the effect of slicing distance and molecular weight (data points were averaged across all polymer concentrations). Lower case Roman numerals are a cross-reference to Panel B. **B)** Representative images of the effect of slicing distance and molecular weight on scaffold height: 300 g/mol with 0.1 μm slicing distance (i), 300 g/mol with 1.5 μm slicing distance (ii), and 900 g/mol with 1.5 μm slicing distance with all other variables held at 50 wt% prepolymer and 0.5 μm hatching distance. Scale bars represent 50 μm. **C)** Pie chart representing the contribution of experimental variables on scaffold height with constant slicing distance of 0.5 μm and a consolidated graphical

analysis showing only the effect of hatching distance and prepolymer concentration (data points were averaged across both molecular weights). In **A** and **C**, the dotted line indicates the designed scaffold height of 120 μm and the colors represent the following variables: red, slicing or hatching distance; orange, interaction between slicing or hatching distance and molecular weight; yellow, molecular weight; green, interaction between molecular weight and prepolymer concentration; blue, prepolymer concentration; purple, interaction between prepolymer concentration and slicing or hatching distance; brown, interaction between slicing or hatching distance, molecular weight and prepolymer concentration; grey, other.

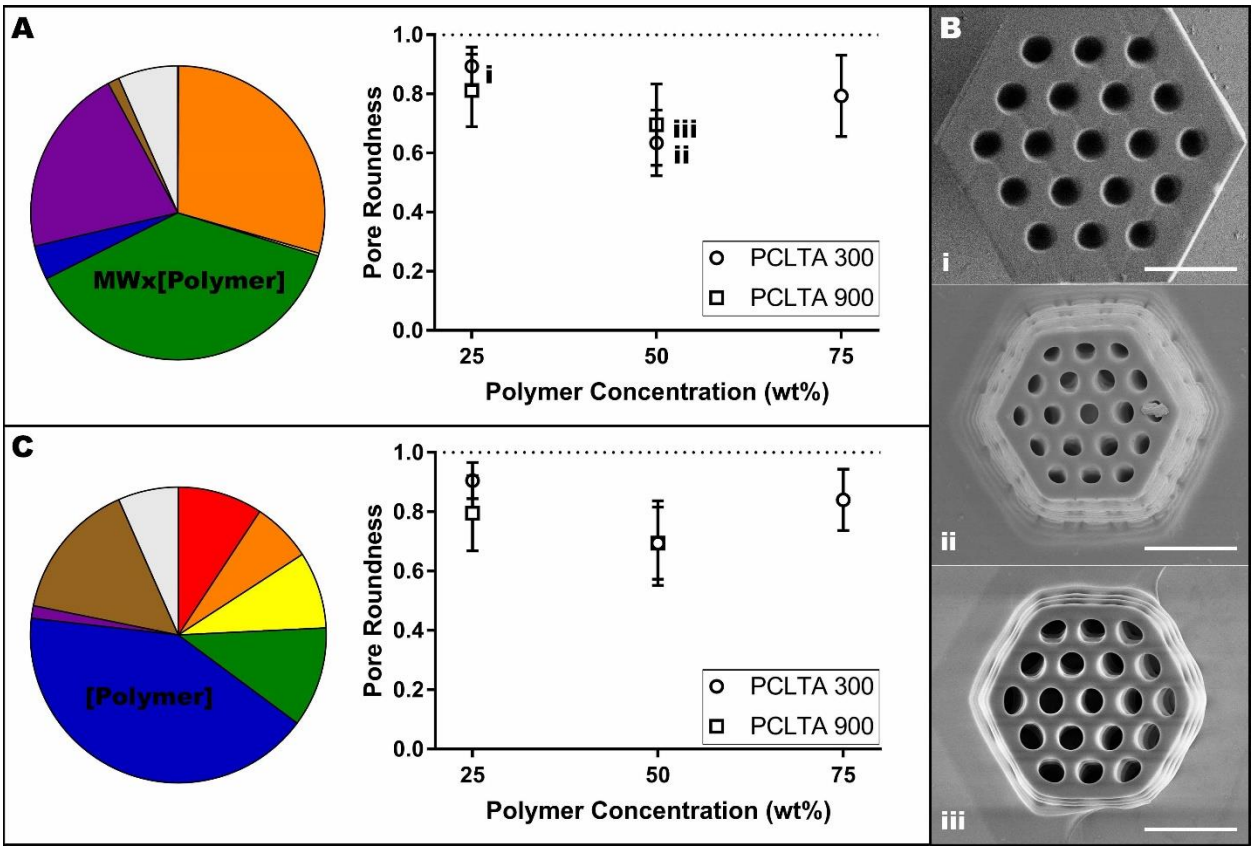

Figure 2.S5: Influence of molecular weight and prepolymer concentration on vertical pore roundness. **A)** Pie chart representing the contribution of experimental variables on pore roundness with constant hatching distance of 0.5 μm and a consolidated graphical analysis showing only the effect of prepolymer concentration and molecular weight (data points were averaged across all slicing distances). . Lower case Roman numerals are a cross-reference to Panel B. **B)** Representative images of the effect of prepolymer concentration and molecular weight on pore roundness: 300 g/mol at 25 wt% (i), 300 g/mol at 50 wt% (ii), and 900 g/mol at 50 wt% with all other variables held constant at 1.5 μm slicing distance and 0.5 μm hatching distance. Scale bars represent 50 μm. **C)** Pie chart representing the contribution of experimental variables on vertical pore roundness with constant slicing distance of 0.5 μm and a consolidated graphical analysis showing

only the effect of molecular weight and prepolymer concentration (data points were averaged across all hatching distances). In **A** and **C**, the dotted line indicates the designed pore roundness of 1.0 and the colors represent the following variables: red, slicing or hatching distance; orange, interaction between slicing or hatching distance and molecular weight; yellow, molecular weight; green, interaction between molecular weight and prepolymer concentration; blue, prepolymer concentration; purple, interaction between prepolymer concentration and slicing or hatching distance; brown, interaction between slicing or hatching distance, molecular weight and prepolymer concentration; grey, other.

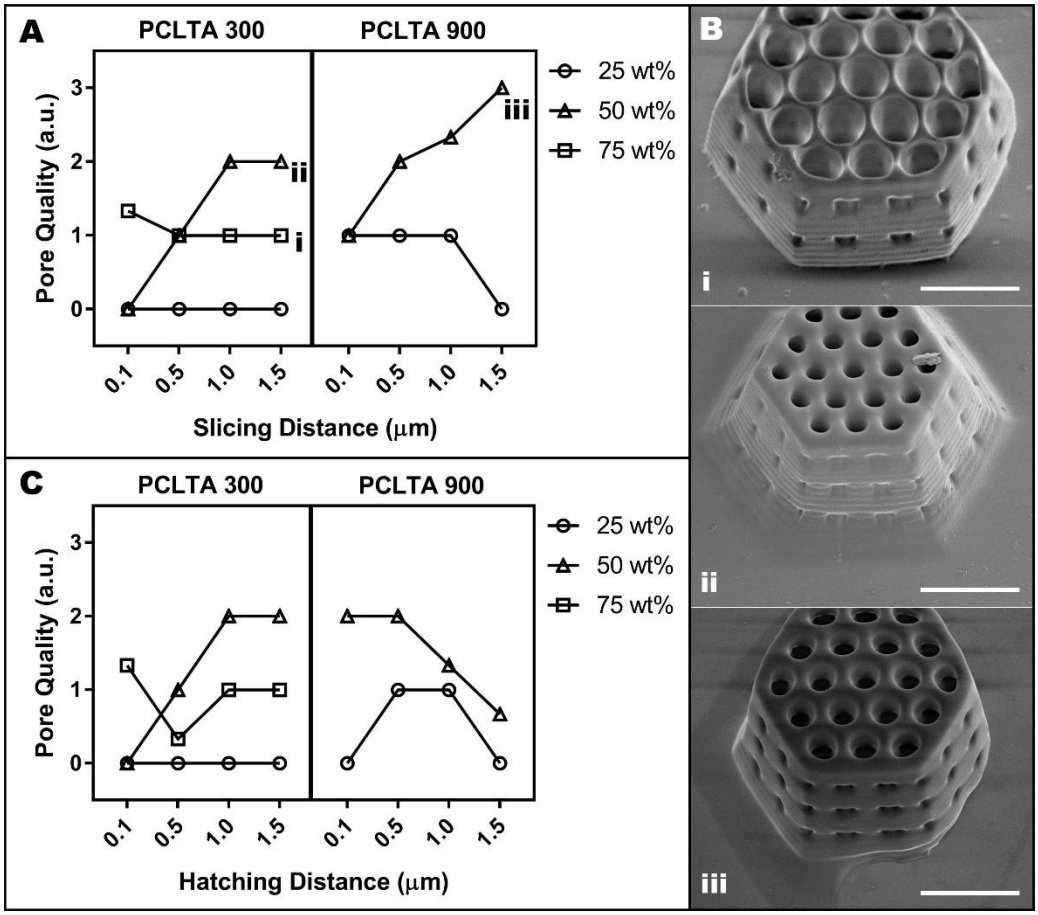

Figure 2.S6: Influence of slicing distance, hatching distance, molecular weight and prepolymer concentration on horizontal pore quality. **A**) Graphical representation of variable contribution to horizontal pore quality with a constant hatching distance of 0.5 μm. Lower case Roman numerals are a cross-reference to Panel B. **B**) Representative images of the effect of prepolymer concentration and molecular weight on pore quality: 300 g/mol at 75 wt% (**i**), 300 g/mol at 50 wt% (**ii**), and 900 g/mol at 50 wt% (**iii**) with all other variables held constant at 1.5 μm slicing distance and 0.5 μm hatching distance. Scale bars represent 50 μm. **C**) Graphical representation of variable contribution to horizontal pore quality with a constant slicing distance of 0.5 μm.

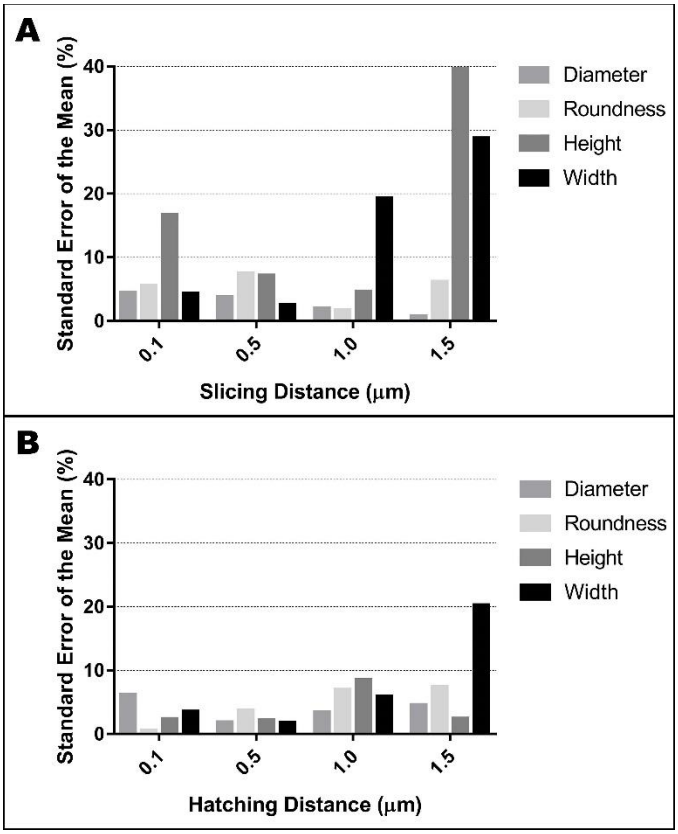

Figure 2.S7: Reproducibility of two-photon polymerized scaffolds. Variation in scaffold features between replicates as a function of slicing distance (**A**) or hatching distance (**B**) with 900 g/mol PCLTA at a concentration of 50 wt% and all other variables held constant.

2.5.3 Tables

Table 2.S1: Statistical analyses of the effects of slicing distance, hatching distance, molecular weight and polymer concentration on scaffold width.

A) Three-way ANOVA showing the effect of slicing distance (0.1 vs. 1.5 μm), molecular weight (300 vs. 900 g/mol) and polymer concentration (25 vs. 50 wt%) a fixed hatching distance of 0.5 μm.		
Source of Variation	% of total variation	P value
Slicing	33.82	< 0.0001
MW	33.04	< 0.0001
[Polymer]	0.000633	0.8493
Slicing x MW	0.6716	< 0.0001
Slicing x [Polymer]	0.7865	< 0.0001
MW x [Polymer]	15.57	< 0.0001
Slicing x MW x [Polymer]	15.83	< 0.0001
B) Two-way ANOVA showing the effect of slicing distance (0.1, 0.5, 1.0 and 1.5 μm) and molecular weight (300 and 900 g/mol) at fixed hatching distance of 0.5 μm and averaged across all polymer concentrations.		
Source of Variation	% of total variation	P value
Slicing	22.55	< 0.0001
MW	36.29	< 0.0001
Slicing x MW	1.616	0.5760
C) Tukey's multiple comparisons test showing the effect of slicing distance at each molecular weight, at fixed hatching distance of 0.5 μm and averaged across all polymer concentrations.		
	Mean Diff.	95% CI of Diff.	Adjusted P Value
300 g/mol			
0.1 vs. 0.5 μm	19.82	-11.42 to 51.07	0.3413
0.1 vs. 1.0 μm	29.25	1.30 to 57.19	< 0.05
0.1 vs. 1.5 μm	31.58	3.63 to 59.52	< 0.05
0.5 vs. 1.0 μm	9.425	-21.82 to 40.67	0.8531
0.5 vs. 1.5 μm	11.75	-19.49 to 43.00	0.7498
1.0 vs. 1.5 μm	2.33	-25.62 to 30.28	0.9961
900 g/mol			
0.1 vs. 0.5 μm	19.09	-15.14 to 53.32	0.4551
0.1 vs. 1.0 μm	39.15	4.92 to 73.38	< 0.05
0.1 vs. 1.5 μm	51.75	17.52 to 85.98	< 0.01
0.5 vs. 1.0 μm	20.06	-14.17 to 54.28	0.4115
0.5 vs. 1.5 μm	32.66	-1.568 to 66.89	0.0665
1.0 vs. 1.5 μm	12.60	-21.62 to 46.83	0.7618

Table S1 (cont'd).

D) Sidak's multiple comparisons test showing the effect of molecular weight (300 vs 900 g/mol) at each slicing distance, at fixed hatching distance of 0.5 μm and averaged across all polymer concentrations.			
Slicing Distance	Mean Diff.	95% CI of Diff.	Adjusted P Value
0.1 μm	33.03	2.646 to 63.41	< 0.05
0.5 μm	32.30	-0.9838 to 65.57	0.0604
1.0 μm	42.93	12.55 to 73.31	<0.01
1.5 μm	53.20	22.82 to 83.58	< 0.001
E) Three-way ANOVA showing the effect of hatching distance (0.1 vs. 1.5 μm), molecular weight (300 vs. 900 g/mol) and polymer concentration (25 vs. 50 wt%) at a fixed slicing distance of 0.5 μm.			
Source of Variation		% of total variation	P value
Hatching		38.79	< 0.0001
MW		39.39	< 0.0001
[Polymer]		2.505	< 0.0001
Hatching x MW		3.224	< 0.0001
Hatching x [Polymer]		3.942	< 0.0001
MW x [Polymer]		7.821	< 0.0001
Hatching x MW x [Polymer]		4.158	< 0.0001
F) Two-way ANOVA showing the effect of slicing distance (0.1, 0.5, 1.0 and 1.5 μm) and molecular weight (300 and 900 g/mol) at fixed slicing distance of 0.5 μm and averaged across all polymer concentrations.			
Source of Variation		% of total variation	P value
Hatching		25.52	< 0.0001
MW		43.84	< 0.0001
Hatching x MW		4.503	< 0.05

Table S1 (cont'd).

G) Tukey's multiple comparisons test showing the effect of hatching distance at each molecular weight, at fixed slicing distance of 0.5 μm and averaged across all polymer concentrations.			
	Mean Diff.	95% CI of Diff.	Adjusted P Value
300 g/mol			
0.1 vs. 0.5 μm	17.92	-6.806 to 42.64	0.2309
0.1 vs. 1.0 μm	24.16	-0.5615 to 48.88	0.0577
0.1 vs. 1.5 μm	31.13	6.405 to 55.85	< 0.01
0.5 vs. 1.0 μm	6.244	-18.48 to 30.97	0.9078
0.5 vs. 1.5 μm	13.21	-11.51 to 37.93	0.4939
1.0 vs. 1.5 μm	6.966	-17.76 to 31.69	0.8772
900 g/mol			
0.1 vs. 0.5 μm	18.69	-11.59 to 48.97	0.3666
0.1 vs. 1.0 μm	43.53	13.26 to 73.81	< 0.01
0.1 vs. 1.5 μm	69.06	38.78 to 99.34	< 0.0001
0.5 vs. 1.0 μm	24.84	-5.433 to 55.12	0.1430
0.5 vs. 1.5 μm	50.37	20.09 to 80.65	< 0.001
1.0 vs. 1.5 μm	25.53	-4.752 to 55.8	0.1267
H) Sidak's multiple comparisons test showing the effect of molecular weight (300 vs 900 g/mol) at each hatching distance, at fixed slicing distance of 0.5 μm and averaged across all polymer concentrations.			
Hatching Distance	Mean Diff.	95% CI of Diff.	Adjusted P Value
0.1 μm	34.10	7.235 to 60.97	< 0.01
0.5 μm	34.88	8.008 to 61.75	< 0.01
1.0 μm	53.48	26.61 to 80.35	< 0.0001
1.5 μm	72.04	45.17 to 98.91	< 0.0001

Table 2.S2: Statistical analyses of the effects of slicing distance, hatching distance, molecular weight and polymer concentration on vertical pore diameter.

A) Three-way ANOVA showing the effect of slicing distance (0.1 vs. 1.5 μm), molecular weight (300 vs. 900 g/mol) and polymer concentration (25 vs. 50 wt%) at a fixed hatching distance of 0.5 μm.			
Source of Variation		% of total variation	P value
Slicing		0.3818	< 0.0001
MW		0.5348	< 0.0001
[Polymer]		1.81	< 0.0001
Slicing x MW		21.57	< 0.0001
Slicing x [Polymer]		10.77	< 0.0001
MW x [Polymer]		61.69	< 0.0001
Slicing x MW x [Polymer]		1.518	< 0.0001
B) Two-way ANOVA showing the effect of molecular weight (300 and 900 g/mol) and polymer concentration (25 and 50 wt%) at fixed hatching distance of 0.5 μm and averaged across all slicing distances.			
Source of Variation		% of total variation	P value
MW		3.314	< 0.0001
[Polymer]		1.088	< 0.05
MW x [Polymer]		52.24	<0.0001
C) Sidak's multiple comparisons test showing the effect of molecular weight (300 vs.900 g/mol) at each polymer concentration, at fixed hatching distance of 0.5 μm and averaged across all slicing distances.			
[Polymer] (wt%)	Mean Diff.	95% CI of Diff.	Adjusted P Value
25	4.726	4.038 to 5.414	< 0.0001
50	-2.825	-3.558 to -2.091	< 0.0001
D) Sidak's multiple comparisons test showing the effect of polymer concentration (25 vs. 50 wt%) at each molecular weight, at fixed hatching distance of 0.5 μm and averaged across all slicing distances.			
MW (g/mol)	Mean Diff.	95% CI of Diff.	Adjusted P Value
300	4.32	3.587 to 5.054	< 0.0001
900	-3.231	-3.919 to -2.542	< 0.0001
E) Tukey's multiple comparisons test (following one-way ANOVA, $p < 0.0001$), showing the effect of polymer concentration (25, 50 and 75 wt%) at fixed molecular weight of 300 g/mol, fixed hatching distance of 0.5 μm and averaged across all slicing distances.			
	Mean Diff.	95% CI of Diff.	Adjusted P Value
25 vs. 50 wt%	4.32	3.233 to 5.407	< 0.0001
25 vs. 75 wt%	-0.1048	-1.101 to 0.8909	0.9664
50 vs. 75 wt%	-4.425	-5.59 to -3.26	< 0.0001

Table S2 (cont'd).

F) Three-way ANOVA showing the effect of hatching distance (0.1 vs. 1.5 μm), molecular weight (300 vs. 900 g/mol) and polymer concentration (25 vs. 50 wt%) at a fixed slicing distance of 0.5 μm.		
Source of Variation	% of total variation	P value
Hatching	1.705	< 0.001
MW	0.7823	< 0.01
[Polymer]	21.8	< 0.0001
Hatching x MW	17.96	< 0.0001
Hatching x [Polymer]	2.316	< 0.0001
MW x [Polymer]	52.29	< 0.0001
Hatching x MW x [Polymer]	1.985	< 0.0001
G) Two-way ANOVA showing the effect of molecular weight (300 and 900 g/mol) and polymer concentration (25 and 50 wt%) at fixed slicing distance of 0.5 μm and averaged across all hatching distances.		
Source of Variation	% of total variation	P value
MW	1.912	< 0.01
[Polymer]	4.707	< 0.0001
MW x [Polymer]	53.09	< 0.0001

H) Sidak's multiple comparisons test showing the effect of molecular weight (300 vs.900 g/mol) at each polymer concentration, at fixed slicing distance of 0.5 μm and averaged across all hatching distances.			
[Polymer] (wt%)	Mean Diff.	95% CI of Diff.	Adjusted P Value
25	5.204	4.443 to 5.965	< 0.0001
50	-3.544	-4.409 to -2.679	< 0.0001

I). Sidak's multiple comparisons test showing the effect of polymer concentration (25 vs. 50 wt%) at each molecular weight, at fixed slicing distance of 0.5 μm and averaged across all hatching distances.			
MW (g/mol)	Mean Diff.	95% CI of Diff.	Adjusted P Value
300	5.676	4.848 to 6.504	< 0.0001
900	-3.072	-3.872 to -2.271	< 0.0001

J) Tukey's multiple comparisons test (following one-way ANOVA, $p < 0.0001$), showing the effect of polymer concentration (25, 50 and 75 wt%) at fixed molecular weight of 300 g/mol, fixed slicing distance of 0.5 μm and averaged across all hatching distances.			
	Mean Diff.	95% CI of Diff.	Adjusted P Value
25 vs. 50 wt%	5.676	4.763 to 6.59	< 0.0001
25 vs. 75 wt%	-1.069	-1.834 to -0.304	< 0.01
50 vs. 75 wt%	-6.746	-7.669 to -5.822	< 0.0001

Table 2.S3: Statistical analyses of the effects of slicing distance, hatching distance, molecular weight and polymer concentration on scaffold height.

A) Three-way ANOVA showing the effect of slicing distance (0.1 vs. 1.5 μm), molecular weight (300 vs. 900 g/mol) and polymer concentration (25 vs. 50 wt%) at a fixed hatching distance of 0.5 μm.		
Source of Variation	% of total variation	P value
Slicing	54.81	< 0.0001
MW	11.88	< 0.0001
[Polymer]	7.841	< 0.0001
Slicing x MW	4.108	< 0.01
Slicing x [Polymer]	1.716	< 0.05
MW x [Polymer]	0.1275	0.4957
Slicing x MW x [Polymer]	15.32	< 0.0001
B) Two-way ANOVA showing the effect of slicing distance (0.1, 0.5, 1.0 and 1.5 mm) and molecular weight (300 and 900 g/mol) at fixed hatching distance of 0.5 μm and averaged across all polymer concentrations.		
Source of Variation	% of total variation	P value
Slicing	45.65	< 0.0001
MW	7.523	< 0.01
Slicing x MW	10.05	< 0.01
C) Tukey's multiple comparisons test showing the effect of slicing distance at each molecular weight, at fixed hatching distance of 0.5 μm and averaged across all polymer concentrations.		
	Mean Diff.	95% CI of Diff.	Adjusted P Value
300 g/mol			
0.1 vs. 0.5 μm	0.8788	-21.08 to 22.84	0.9996
0.1 vs. 1.0 μm	15.1	-4.538 to 34.74	0.1859
0.1 vs. 1.5 μm	22.86	3.215 to 42.5	< 0.05
0.5 vs. 1.0 μm	14.22	-7.735 to 36.18	0.3232
0.5 vs. 1.5 μm	21.98	0.0181 to 43.94	< 0.05
1.0 vs. 1.5 μm	7.753	-11.89 to 27.39	0.7212
900 g/mol			
0.1 vs. 0.5 μm	7.178	-16.88 to 31.23	0.8570
0.1 vs. 1.0 μm	18.96	-5.095 to 43.01	0.1687
0.1 vs. 1.5 μm	61.62	37.57 to 85.68	< 0.0001
0.5 vs. 1.0 μm	11.78	-12.27 to 35.84	0.5657
0.5 vs. 1.5 μm	54.44	30.39 to 78.5	< 0.0001
1.0 vs. 1.5 μm	42.66	18.61 to 66.72	< 0.001

Table S3 (cont'd).

D) Sidak's multiple comparisons test showing the effect of molecular weight (300 vs 900 g/mol) at each slicing distance, at fixed hatching distance of 0.5 μm and averaged across all polymer concentrations.			
Slicing Distance	Mean Diff.	95% CI of Diff.	Adjusted P Value
0.1 μm	1.164	-20.19 to 22.51	0.9998
0.5 μm	7.463	-15.93 to 30.85	0.8815
1.0 μm	5.021	-16.33 to 26.37	0.9575
1.5 μm	39.93	18.58 to 61.28	< 0.0001
E) Three-way ANOVA showing the effect of hatching distance (0.1 vs. 1.5 μm), molecular weight (300 vs. 900 g/mol) and polymer concentration (25 vs. 50 wt%) at a fixed slicing distance of 0.5 μm.			
Source of Variation		% of total variation	P value
Hatching		15.04	< 0.001
MW		0.8232	0.2799
[Polymer]		45.44	< 0.0001
Hatching x MW		9.935	< 0.01
Hatching x [Polymer]		0.9341	0.2509
MW x [Polymer]		1.022	0.2306
Hatching x MW x [Polymer]		16.28	< 0.001
F) Two-way ANOVA showing the effect of hatching distance (0.1, 0.5, 1.0 and 1.5 μm) and polymer concentration (25, 50 and 75 wt%) at fixed slicing distance of 0.5 μm and averaged across both molecular weights.			
Source of Variation		% of total variation	P value
Hatching		22.2	< 0.0001
[Polymer]		38.34	< 0.0001
Hatching x [Polymer]		5.055	0.3350

Table S3 (cont'd).

G) Tukey's multiple comparisons test showing the effect of hatching distance at each polymer concentration, at fixed slicing distance of 0.5 μm and averaged across both molecular weights.			
	Mean Diff.	95% CI of Diff.	Adjusted P Value
25 wt%			
0.1 vs. 0.5 μm	-0.01076	-22.58 to 22.56	> 0.9999
0.1 vs. 1.0 μm	2.534	-20.04 to 25.11	0.9906
0.1 vs. 1.5 μm	17.21	-5.359 to 39.79	0.1916
0.5 vs. 1.0 μm	2.545	-20.03 to 25.12	0.9905
0.5 vs. 1.5 μm	17.23	-5.349 to 39.8	0.1911
1.0 vs. 1.5 μm	14.68	-7.893 to 37.25	0.3193
50 wt%			
0.1 vs. 0.5 μm	14.31	-8.266 to 36.88	0.3417
0.1 vs. 1.0 μm	27.69	5.116 to 50.26	< 0.05
0.1 vs. 1.5 μm	28.64	6.07 to 51.22	< 0.01
0.5 vs. 1.0 μm	13.38	-9.193 to 35.96	0.4008
0.5 vs. 1.5 μm	14.34	-8.239 to 36.91	0.3400
1.0 vs. 1.5 μm	0.9539	-21.62 to 23.53	0.9995
75 wt%			
0.1 vs. 0.5 μm	21.15	-10.77 to 53.07	0.3034
0.1 vs. 1.0 μm	34.23	2.31 to 66.16	< 0.05
0.1 vs. 1.5 μm	43.7	11.78 to 75.63	< 0.01
0.5 vs. 1.0 μm	13.08	-18.84 to 45.01	0.6968
0.5 vs. 1.5 μm	22.55	-9.373 to 54.48	0.2501
1.0 vs. 1.5 μm	9.467	-22.46 to 41.39	0.8590

Table S3 (cont'd).

H) Tukey's multiple comparisons test showing the effect of polymer concentration at each hatching distance, at fixed slicing distance of 0.5 μm and averaged across both molecular weights.			
	Mean Diff.	95% CI of Diff.	Adjusted P Value
0.1 μm			
25 vs. 50 wt%	-45.57	-66.08 to -25.06	< 0.0001
25 vs. 75 wt%	-23.88	-49.01 to 1.241	0.0655
50 vs. 75 wt%	21.69	-3.438 to 46.81	0.1031
0.5 μm			
25 vs. 50 wt%	-31.25	-51.76 to -10.74	< 0.01
25 vs. 75 wt%	-2.722	-27.85 to 22.4	0.9629
50 vs. 75 wt%	28.53	3.404 to 53.65	< 0.05
1.0 μm			
25 vs. 50 wt%	-20.41	-40.93 to 0.09971	0.0514
25 vs. 75 wt%	7.817	-17.31 to 32.94	0.7336
50 vs. 75 wt%	28.23	3.107 to 53.36	< 0.05
1.5 μm			
25 vs. 50 wt%	-34.14	-54.65 to -13.63	< 0.001
25 vs. 75 wt%	2.604	-22.52 to 27.73	0.9660
50 vs. 75 wt%	36.74	11.62 to 61.87	< 0.01

Table 2.S4: Statistical analyses of the effects of slicing distance, hatching distance, molecular weight and polymer concentration on vertical pore roundness.

A) Three-way ANOVA showing the effect of slicing distance (0.1 vs. 1.5 μm), molecular weight (300 vs. 900 g/mol) and polymer concentration (25 vs. 50 wt%) at a fixed hatching distance of 0.5 μm.			
Source of Variation		% of total variation	P value
Slicing		0.06699	0.3694
MW		0.3022	0.0588
[Polymer]		3.761	< 0.0001
Slicing x MW		29.37	< 0.0001
Slicing x [Polymer]		20.79	< 0.0001
MW x [Polymer]		37.85	< 0.0001
Slicing x MW x [Polymer]		1.279	< 0.001
B) Two-way ANOVA showing the effect of molecular weight (300 and 900 g/mol) and polymer concentration (25 and 50 wt%) at fixed hatching distance of 0.5 μm and averaged across all slicing distances.			
Source of Variation		% of total variation	P value
MW		0.1097	0.4990
[Polymer]		37.67	< 0.0001
MW x [Polymer]		5.502	< 0.0001
C) Sidak's multiple comparisons test showing the effect of molecular weight (300 vs.900 g/mol) at each polymer concentration, at fixed hatching distance of 0.5 μm and averaged across all slicing distances.			
[Polymer] (wt%)	Mean Diff.	95% CI of Diff.	Adjusted P Value
25	0.08169	0.03572 to 0.1277	< 0.001
50	-0.06147	-0.1105 to -0.01246	< 0.05
D) Sidak's multiple comparisons test showing the effect of polymer concentration (25 vs. 50 wt%) at each molecular weight, at fixed hatching distance of 0.5 μm and averaged across all slicing distances.			
MW (g/mol)	Mean Diff.	95% CI of Diff.	Adjusted P Value
300	0.2589	0.2099 to 0.3079	< 0.0001
900	0.1157	0.06975 to 0.1617	< 0.0001
E) Tukey's multiple comparisons test (following one-way ANOVA, $p < 0.0001$), showing the effect of polymer concentration (25, 50 and 75 wt%) at fixed molecular weight of 300 g/mol, fixed hatching distance of 0.5 μm and averaged across all slicing distances.			
	Mean Diff.	95% CI of Diff.	Adjusted P Value
25 vs. 50 wt%	0.2589	0.2111 to 0.3067	<0.0001
25 vs. 75 wt%	0.09996	0.05617 to 0.1438	<0.0001
50 vs. 75 wt%	-0.1589	-0.2102 to -0.1077	<0.0001

Table S4 (cont'd).

F) Three-way ANOVA showing the effect of hatching distance (0.1 vs. 1.5 μm), molecular weight (300 vs. 900 g/mol) and polymer concentration (25 vs. 50 wt%) at a fixed slicing distance of 0.5 μm.		
Source of Variation	% of total variation	P value
Slicing	9.28	< 0.001
MW	8.415	< 0.001
[Polymer]	41.65	< 0.0001
Slicing x MW	6.545	< 0.01
Slicing x [Polymer]	1.369	0.0875
MW x [Polymer]	10.92	< 0.0001
Slicing x MW x [Polymer]	15.22	< 0.0001
G) Two-way ANOVA showing the effect of molecular weight (300 and 900 g/mol) and polymer concentration (25 and 50 wt%) at fixed slicing distance of 0.5 μm and averaged across all hatching distances.		
Source of Variation	% of total variation	P value
MW	3.602	< 0.001
[Polymer]	28.89	< 0.0001
MW x [Polymer]	3.68	< 0.001

H) Sidak's multiple comparisons test showing the effect of molecular weight (300 vs.900 g/mol) at each polymer concentration, at fixed slicing distance of 0.5 μm and averaged across all hatching distances.			
[Polymer] (wt%)	Mean Diff.	95% CI of Diff.	Adjusted P Value
25	0.1107	0.06443 to 0.157	< 0.0001
50	-0.000594	-0.05318 to 0.05199	0.9996

I) Sidak's multiple comparisons test showing the effect of polymer concentration (25 vs. 50 wt%) at each molecular weight, at fixed slicing distance of 0.5 μm and averaged across all hatching distances.			
MW (g/mol)	Mean Diff.	95% CI of Diff.	Adjusted P Value
300	0.2116	0.1612 to 0.2619	< 0.0001
900	0.1003	0.05157 to 0.149	< 0.0001

J) Tukey's multiple comparisons test (following one-way ANOVA, $p < 0.0001$), showing the effect of polymer concentration (25, 50 and 75 wt%) at fixed molecular weight of 300 g/mol, fixed slicing distance of 0.5 μm and averaged across all hatching distances.			
	Mean Diff.	95% CI of Diff.	Adjusted P Value
25 vs. 50 wt%	0.2116	0.1681 to 0.255	< 0.0001
25 vs. 75 wt%	0.06582	0.02941 to 0.1022	< 0.0001
50 vs. 75 wt%	-0.1458	-0.1897 to -0.1018	< 0.0001

Table 2.S5: Statistical analyses of the effects of slicing distance, hatching distance, molecular weight and polymer concentration on horizontal pore quality.

A) Mean differences showing the effect of slicing distance (0.1 vs. 1.5 μm), molecular weight (300 vs. 900 g/mol) and polymer concentration (25 vs. 50 wt%) at a fixed hatching distance of 0.5 μm. Analysis of variance could not be performed because there was no variation among replicates for each condition.	
Source of Variation	Mean Difference
Slicing	0.75
MW	0.75
[Polymer]	1.25

B) Three-way ANOVA showing the effect of hatching distance (0.1 vs. 1.5 μm), molecular weight (300 vs. 900 g/mol) and polymer concentration (25 vs. 50 wt%) at a fixed slicing distance of 0.5 μm.		
Source of Variation	% of total variation	P value
Hatching	0.9346	0.0628
MW	0.9346	0.0628
[Polymer]	45.79	< 0.0001
Slicing x MW	23.36	< 0.0001
Slicing x [Polymer]	0.9346	0.0628
MW x [Polymer]	0.9346	0.0628
Slicing x MW x [Polymer]	23.36	< 0.0001

Table 2.S6: List of tissues harvested and examined for evaluation of systemic toxicity and tumorigenicity.

Aorta	Pancreas
Adrenals	Pituitary
Bone with bone marrow, femur	Reproductive tract
Bone with bone marrow, sternum	Salivary gland, mandibular + Parotid
Brain	Skeletal muscle
Esophagus	Skin
Eye with optic nerve	Small intestine
Heart	Spinal cord, cervical
Inguinal fat pad with mammary tissue	Spinal cord, lumbar
Kidney L/R	Spinal cord, thoracic
Lacrimal gland	Spleen
Large intestine, cecum	Sternum
Large intestine, colon	Stomach
Larynx	Thymus
Liver	Thyroid
Lung L/R	Tongue
Lymph node, mandibular	Trachea
Nerve, sciatic	Ureters

CHAPTER III: PURIFICATION OF ACRYLATED PCL

3.1 Introduction

As previously stated, the ability to photopolymerize PCL enables fabrication via two-photon lithography, which can result in intricate tissue scaffolds for cell replacement therapy. When creating a new implant, the materials, fabrication, handling procedure, and sterilization must be thoroughly considered before meeting the approval of regulating agencies such as the Food and Drug Administration (FDA). Cytotoxicity is a main concern when producing a material that has not been used in a medical device before. And although linear PCL has been used in some already clinically-approved devices,[21] the synthesis necessary to incorporate acrylates introduces new chemicals, thus new procedures that must be standardized. A reliable method to calculate the success of the reaction, i.e. the percent of alcohol groups replaced with acrylate groups, must be measurable in order to develop a standard operating procedure with adequate quality control.

In this work, various combinations of evaporation and phase separation with water or concentrated sodium bicarbonate were investigated as a means to remove acryloyl chloride and acrylic acid from polycaprolactone triacrylate (PCLTA). In addition to the phase separations, the effects of different modes of agitation (manual shaking or magnetic stirring) on purification efficacy were determined. The procedure developed here enables us and other researchers to reliably and reproducibly purify PCLTA, facilitating its use in various biomedical devices and materials.

3.2 Methods

3.2.1 PCL Functionalization

PCL triol was functionalized with acrylates using a modified protocol based on a commonly used synthesis method.[33] Potassium carbonate (KCO_3) was dried in an oven over night at 74 °C. PCL triol (300 or 900 g/mol), acryloyl chloride, and dichloromethane (DCM) (Sigma-Aldrich, St. Louis, MO) were used as received. About 20 grams of PCL triol were dissolved in excess of DCM, approximately 200 mL, with 1.5 molar ratio of KCO_3 to alcohol groups. The reaction was stirred to suspend the KCO_3, corked with a rubber stopper, and vented to atmosphere (chemical fume hood) with a 20-gauge needle (Becton-Dickinson & Co., Franklin Lakes, NJ). Acryloyl chloride (equimolar to KCO_3) was diluted in DCM at 1:5 (v/v) before being added dropwise into the mixture using a glass syringe. The reaction proceeded for 24 hrs at room temperature. Once complete, the mixture was filtered to remove the solids, specifically KCO_3, KCl, and $KHCO_3$.

3.2.2 PCL Purification

Rotary Evaporator

A rotary evaporator (Hei-VAP Value, Heidolph Instruments GmbH & Co. KG, Schwabach, Germany) was used to remove the DCM at either 60 °C (control) or 73 °C depending on the test conditions. Once condensation was no longer visually detected (0.5 to 1 hr), the product was removed from the evaporation flask and transferred to a 20 mL scintillation vial, then stirred overnight to remove any residual DCM.

Phase Separation

A solution of concentrated sodium bicarbonate ($NaHCO_3$, Research Products International, Mount Prospect, IL) was prepared by combining approximately 100 g of

$NaHCO_3$ and 1 L of distilled water. The PCLTA reaction products were mixed with an aqueous solution of either distilled water or saturated $NaHCO_3$.

For the initial experiment, to determine the method to remove acryloyl chloride, a very small amount of rotary evaporated product was tested (approximately 1 mL) and washed three times in excess aqueous solution. Due to the small quantity, the samples were washed in a 10 mL vial, without using a separatory funnel, and manually shaken to combine phases. Then samples of each trial were collected for NMR.

In the agitation experiments, the unevaporated organic product and aqueous phases were mixed by inversion and gently shaking the separatory funnel or on a magnetic stir plate for an hour in a covered beaker. After mixing, the solution was returned to or left in the separatory funnel to divide, and the organic component was collected for future steps. The product was washed and separated 3 to 5 times before rotary evaporation, as described above, and nuclear magnetic resonance evaluation.

3.2.3 Reaction Validation and Analysis

Success of the reaction and purification was determined with ^1H nuclear magnetic resonance (NMR, Avance-300 NMR Spectrometer, Bruker, Billerica, MA). The functionalized PCL product was dissolved in deuterated chloroform (Sigma-Aldrich), and a field strength of 300 MHz was used to acquire the spectra. The integral of the peaks indicative of acrylates (at δ 5.8, 6.1, and 6.4 ppm) were measured relative to the unreacted methyl peak (at δ 0.9 ppm) to quantify the number of acrylate groups per PCL molecule.

3.3 Results

3.3.1 Method of Reactant Removal

Following reaction completion, the functionalized PCL still contained excess acryloyl chloride as determined by the NMR spectra and integration value (**Figure 3.1-2)**, control). The acrylate groups chemical shift values are between 5.5 and 6.75 ppm and can be described as a triplet of a multiplet. In the control there are two peaks with large integrations trailing (i.e., at higher chemical shifts relative to) the acrylate peaks, and under further observation there is extra splitting of the peaks in the middle of the acrylate multiplet as well. These extra peaks in and trailing the acrylate peaks were hypothesized to be attributed to the excess acryloyl chloride. The integration value of the methyl peak at 0.9 ppm is known to be 3 because there is only methyl on the PCLTA molecule with 3 hydrogens bonded to it. The acrylate peaks were measured relative to this methyl peak, if the reaction were 100% successful the maximum integration of the acrylate peaks would be 9 (**Figure 3.1**). However, the spectra show both extra peaks in the acrylate region and an integration value greater than 9, indicating excess acrylate groups remained in solution. In an effort to remove this reactive molecule from the product, three test conditions were evaluated: a rotary evaporating session at a higher temperature, a phase separation with distilled water, or a phase separation with concentrated sodium bicarbonate, with each separation followed by standard rotary evaporation.

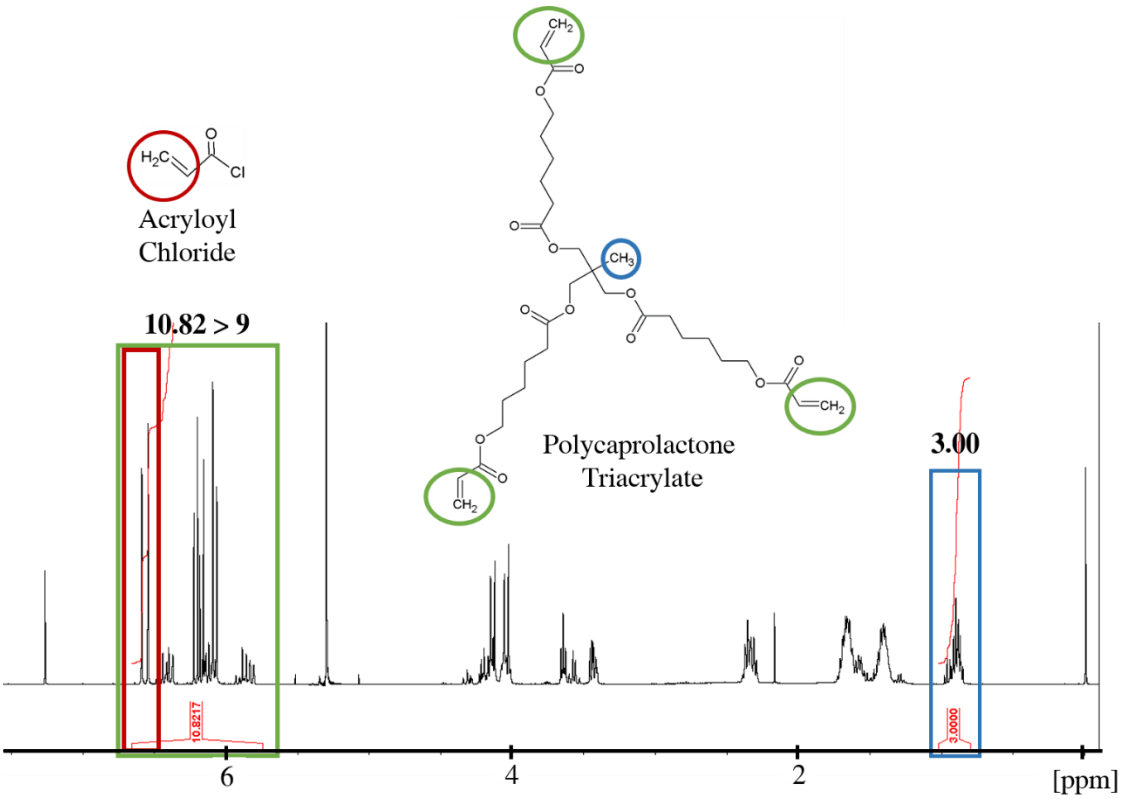

Figure 3.1: Integration of acrylate peaks relative to methyl peaks. Representative NMR spectra with the methyl group on both the molecule and its corresponding peaks labeled blue (3H), the acrylate groups labelled green (9H max), and the assumed acryloyl chloride contamination is red (3H).

.

The resulting peaks from ^{1}H NMR were observed and compared between the test conditions, with a focus on the acrylate peaks (**Figure 3.2A**). The elevated rotary evaporating (rotovap) did not appear to efficiently purify of our product, as determined by the persisting presence of the acryloyl chloride peaks and an integration value greater than 9. The washes with water improved the purity of the product; there was a noticeable reduction in intensity of the trailing peaks and integration was in a realistic range.

However, after three washes and separations with water there were still remnants of the peaks, representing acryloyl chloride, in the sample. The sodium bicarbonate washes resulted in complete removal of the acryloyl chloride peaks from the NMR and, again, presented a realistic measure of the degree of substitution (integration < 9).

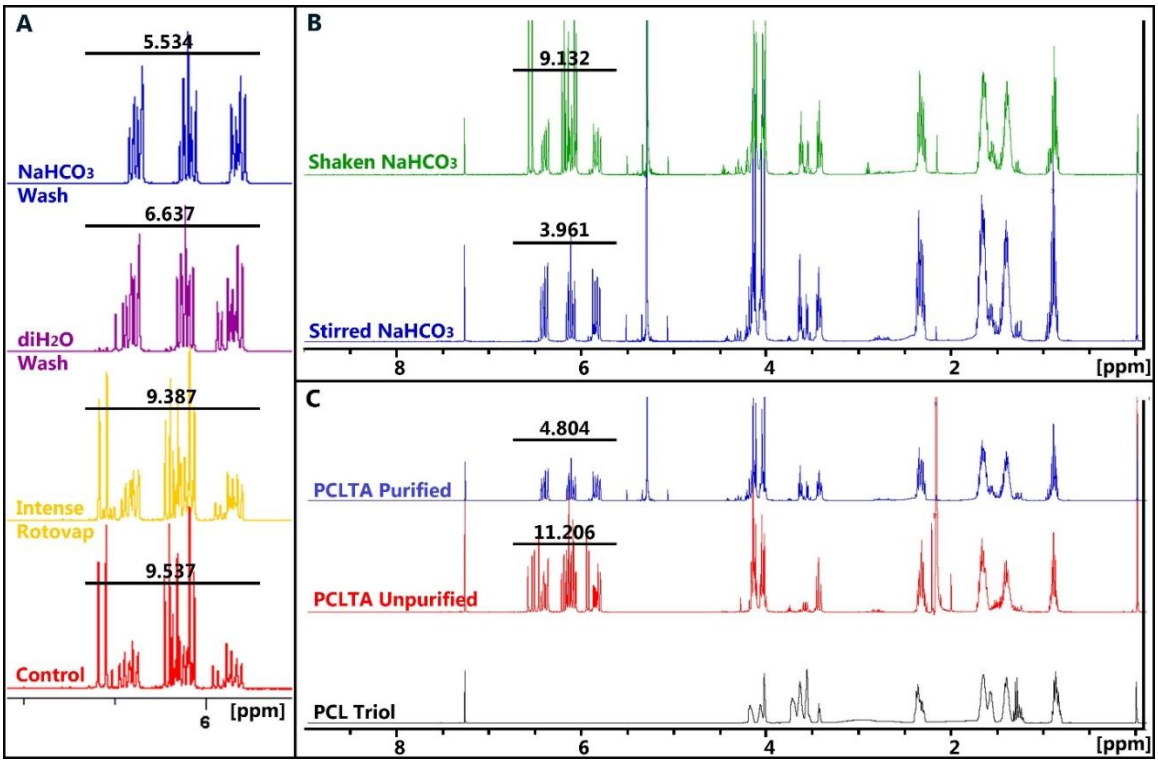

Figure 3.2: Chemical shifts and sample purity. **A)** After synthesis, the products still contain excess reactant, acryloyl chloride, as indicated by peaks trailing the acrylate peaks (control, red) and the greater than 9 integration value (relative to the 0.9 ppm peaks set to an integration of 3). Rotary evaporation at increased temperature (72°C, yellow) failed to remove excess acryloyl chloride. A series of five washes and phase separations with either distilled water (purple) or concentrated sodium bicarbonate solution (blue) were more effective than rotary evaporation alone. **B)** Manual agitation (green) of organic and aqueous phases was less effective than magnetic stirring of the solution. **C)**

A summary of the full NMR spectra for unreacted PCL triol (black), PCLTA before purification (red), and PCLTA after five stirred washes with $NaHCO_3$ (blue).

3.3.2 Method of Agitation

When using a large batch of PCL product (> 10 mL), two methods of agitation were studied as means to combine the organic and aqueous phases. The first method was manual shaking and inverting of a 250 mL separatory funnel containing the product and sodium bicarbonate solution. The second method was magnetically stirring the product with the sodium bicarbonate solution in a covered beaker for an hour at a time. Separations were left as long as necessary for the two phases to divide, and five washes were done for each method. When the PCLTA batch size was increased, the shaken sodium bicarbonate solution maintained the peaks indicative of acryloyl chloride (**Figure 3.2B**). However, the stirred solution resulted in the successful removal of the excess reactants.

Combining the results from the two previous experiments, a final purification was executed using the methods that provided the most pure product. The NMR spectra of the pure PCL triol, PCLTA before purification, and PCLTA after purification were captured to compare the overall change in chemical shifts as the reaction progressed (**Figure 3.2C**). The degree of functionalization of the reaction, as measured by the number of alcohol groups successfully replaced with acrylate groups, can be measured using the integration values of acrylates compared to the known one methyl group. A ratio of 9 acrylate associated hydrogens to 3 methyl bound hydrogens would be representative of a 100% successful reaction. Without the purification steps, the ratio was 11.206 : 3. The

number of hydrogens associated with acrylate groups estimated on the PCLTA was reported greater than possible based on the number of reactive sites on the PCL triol molecule. After the sodium bicarbonate washes, the product has a ratio of 4.804 : 3, representative of a 46% successful replacement of alcohol groups with acrylates.

3.4 Discussion

Polycaprolactone is an advantageous material to select for implant design because it is biodegradable, biocompatible, and utilized in established FDA-approved devices currently on the market. Polycaprolactone functionalized with acrylate groups enables it to be used for photopolymerization methods, which allows for microstructuring of the polymer for tissue scaffold design. An optimized method of synthesizing and purifying PCLTA is necessary to establish a quality and control standard when moving forward in the FDA approval process of a medical device.

In this work, sodium bicarbonate washes were found to be superior at removing acryloyl chloride and acrylic acid from the PCLTA product than the distilled water washes or increased temperature rotary evaporation. Although the boiling point of acryloyl chloride is only 75 °C, the extent to which the temperature of the rotary evaporation treatment could be increased was limited because high temperatures cause PCLTA to polymerize. A great enough temperature to boil off acryloyl chloride and acrylic acid (b.p. 141 °C) could not be achieved without risking polymerization of the polymer. Therefore, the excess reactant was not successfully removed from the product with this method. The washes and separations using distilled water showed evidence of partial removal of the acrylic acid and acryloyl chloride, whereas the concentrated sodium bicarbonate solution was very successful at removing the excess reactants.

Acryloyl chloride is not very soluble in aqueous solutions, but once the chloride has reacted with water, the resulting acrylic acid preferentially dissolves in water. The sodium bicarbonate functions as a driver for this reaction, neutralizing the acrylic and hydrochloric acid and thus maintaining a chemical gradient that encourages the acryloyl chloride to react with water. The washes with sodium bicarbonate were superior to the water because the gradient was more favorable to remove the acrylic acid and acryloyl chloride. The washes with water could achieve a similar effect after a greater number of washes.

Another way to increase the efficiency of the purification step was increasing the degree of agitation between the two phases. Stirring the solutions together on a stir plate for a longer period of time was more effective at removing the acryloyl chloride than manually shaking. The stirring was more effective because it incorporated the phases together for a longer period of time (1 hr), and the incessant stirring allowed for a higher quantity of low-volume micelles to form. This increase in micelles, and decrease in micelle volume, resulted in a greater surface area to volume ratio for the two phases to interact and remove the acryloyl chloride.

The final batch of PCLTA concocted using the new protocol had a low degree of substitution, with only 46% of the alcohol groups becoming functionalized with acrylate groups. We hypothesize that this low extent of reaction is due to moisture in the reaction system. Namely, the oven used is multipurpose and shared with multiple nearby labs, primarily to dry autoclaved glassware. The humidity present in the oven from drying these supplies and equipment likely hydrated the KCO_3, precisely the opposite of the desired outcome. Since the KCO_3 in this reaction is meant to keep the reaction dry, its

hydration from the oven likely caused it to be less effective at removing water during the synthesis. Thus, the water that did enter the system could react with the acryloyl chloride and quench the reaction. To increase the number of acrylates on the PCL in subsequent work, we have chosen to use anhydrous potassium carbonate as received and have removed the oven dehydration step. This change has increased the degree of substitution to 60-70% (**Figure 3.S1**).

In all, purifying the PCLTA allows for accurate quantification of the number of acrylates that were incorporated per molecule. Knowing the degree of acrylation is important for quality control between different batches of synthesis and the consistency in materials fabricated from the PCLTA. An effective and consistent synthesis procedure has been developed, and will be utilized in future studies for FDA approval of a cell replacement therapy device for the retina.

3.5 Supplemental Information

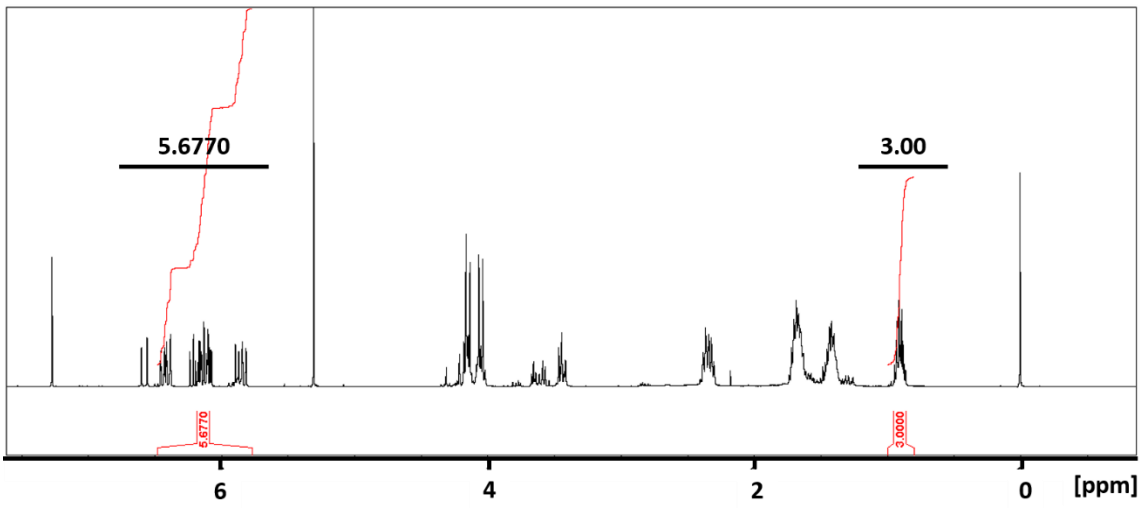

Figure 3.S1: Improved substitution of acrylates. NMR spectra depicting the improved synthesis of PCLTA with a 63% successful substitution of acrylates for alcohol groups.

CHAPTER IV: UV POLYMERIZED TWO DIMENSIONAL SCAFFOLDS

4.1 Introduction

The potential of 3D printed biomaterials is incredibly compelling because of the ability to control the structure, shape, and porosity of medical devices like photoreceptor tissue scaffolds. However, the fabrication time of these methods can be lengthy, and the process to achieve approval of a new device from regulatory agencies like the Food and Drug Administration (FDA) is rigorous and time consuming. All the while, there are patients in need of treatments to restore their quality of life. If there is a device already on the market that is of substantial equivalence to the proposed new device, the process leading up to clinical trials may be expedited.

In comparison to two-photon polymerization, traditional UV polymerization (i.e., flood curing) enables rapid fabrication, but does not facilitate control of material microstructure. This control is especially important, however, for regeneration in neural tissues like the retina, where synapse formation with remaining host cells is crucial to therapeutic success. Incorporating pores into the film allows for the cells to be loaded into the scaffold, to polarize, and to align in native tissue properly, eventually forming synapses with the remaining tissue. This challenge to the use of UV polymerization can theoretically be addressed by restricting light exposure only to desired polymerization areas using a photomask. These light-restricting devices can be created by simply depositing dark regions on an otherwise transparent material (e.g., a glass slide). When the photomask is placed between the light source and the mixture of monomer and photoinitiator, it creates user-controlled shadows on the underlying mixture, preventing polymerization therein.

In this chapter, we determined the UV polymerization parameters that contributed to pore formation in photomasked polycaprolactone films. Specifically, we delineated the minimum light intensity and exposure time needed for film formation and characterized the effect of these conditions on pore diameter and penetration through the thickness of the film. Finally, we studied their compatibility with human induced pluripotent stem cell-derived retinal progenitor cells. We expect that our findings for scaffolds created using this method will help clear the way for regulatory approval of two-photon polymerized triacrylated polycaprolactone devices in the future.

4.2 Methods

4.2.1 Photomasked Film Fabrication

Triacrylated polycaprolactone (PCLTA) was synthesized using the methods developed in Chapter III. A solution of 75 wt% PCLTA 300 g/mol and 25 wt% dioxane (Sigma-Aldrich, St. Louis, MO) was prepared. Irgacure 2959, of the chemical name 1-[4-(2-Hydroxyethoxy)-phenyl]-2-hydroxy-2-methyl-1-propane-1-one (Ciba Specialty Chemicals, Basel, Switzerland), was added as a photoinitiator to the solution at 0.1 wt%.

A laminate mold was constructed beginning with one glass slide and placing two approximately 25 μm thick aluminum spacers on each end of the slide, leaving the center of the slide open. The photomask (hereafter known as "PM," Applied Image Inc., Rochester, NY) was designed with hexagonally-packed 75 μm diameter chromium dots with 25 μm distance from dot edge to dot edge. This photomask was placed centered, chromium side down on top of the spacers and slide. The stack of slides and spacers was clamped together at the ends using one-inch binder clips. Approximately 60 μL of the

PCLTA solution was carefully pipetted between the PM and glass slide. The prepolymer was cured 2 inches from the light source (OmniCure Series 2000 Lamp, Excelitas Technologies, Waltham, MA) using variable light intensities (0.5, 1.0, 1.5, 2.0, and 2.5 W/cm^2) for variable lengths of time (5 to 30 s in increments of 2.5 s) depending on the test conditions. The mold was then gently deconstructed to observe and collect the polymer sample. The exposure time at which the polymer first formed a gel and first formed a film were recorded for each intensity increment.

If the polymer formed a film, it was transferred to a vial containing 10 mL of dioxane. The vial was capped and immediately shaken for 30 seconds on a vortex (IKA Works, Inc, Wilmington, NC) on medium setting to remove unreacted prepolymer and solvent. Vials were left on an orbital shaker (Orbi-Blotter™, Benchmark Scientific, Sayreville, NJ) overnight at room temperature.

Films were gradually moved from dioxane to 1x phosphate buffered saline (PBS) through serial dilutions. Briefly, the films were transferred from their vials to cell strainers made of a polypropylene frame and nylon mesh of arbitrary size (Corning Falcon, Corning, NY) and placed into a recrystallization dish containing a 1:3 dilution of PBS to dioxane (10 mL of solution per sample). The films were next rinsed in a 1:1 dilution, followed by a 3:1 (PBS: dioxane) dilution. Each wash occurred for one hour on an orbital shaker in a chemical fumehood. Finally, the films were placed into a 100% PBS solution. After an hour, the films were transferred to a 12-well plate of fresh PBS for storage at room temperature in preparation for future experiements.

4.2.2 Dynamic Mechanical Analysis

A dynamic mechanical analyzer (DMA Q800 V7.0 Build 113, TA Instruments, New Castle, DE) was used to measure compressive properties of the films made at each intensity with the shortest exposure time, in triplicate. A 4 mm biopsy punch was collected from each film, and the resulting disc was removed from PBS and placed in the submersion compression clamp in static mode. The equipment was operated as specified in the user's manual. The compressive force and distance were recorded for each sample at 20°C, as previously described.[34] Briefly, beginning with a preload force of 0.1 mN, increased force was applied to the sample at a rate of 0.02 N/min with displacement data collected every 2 seconds until a final compression of 0.2 N was achieved. This data was used to calculate the compressive modulus of each sample. Mean and standard deviation were calculated for the moduli at each intensity/time pair.

4.2.3 Confocal Microscopy

Three samples from each group were punched into 4 mm discs, as previously described, and transferred in a bleb of PBS to a coverslip with a transfer pipette. Autofluorescent images and z-stacks were captured with a Leica DM 2500 SPE confocal microscope (Leica Microsystems, Wetzlar, Germany). A volume rendering was acquired from the Lecia software without interpolation and at the default thresholding parameters.

ImageJ (1.48v) was used to measure pore diameter at each layer of the z-stack. Briefly, an imported sequence of images was thresholded with the Color Threshold function using the default settings. Noise was removed using the Remove Outliers function, for both the bright and dark, set at pixels 2 wide in radius and threshold of 50. The image was filtered with the Gaussian Blur 3D with each coordinate parameter set to

2.0. Data was collected from the image sequence using Analyze Particles, with particles restricted to area 800 – infinity μm^2 and circularity 0.5 – 1. The resulting major and minor axes of a fit ellipse were averaged to and assumed to represent the pore diameter at that location. The mean and standard deviation of pore diameter were calculated for each of the z-stack layers.

4.2.4 Scaffold Preparation and Cell Loading

Stored PCLTA samples were wrapped with parafilm, to prevent evaporation of PBS, and placed in two autoclave bags to prepare for gamma irradiation. All radiation treatments were performed at the Radiation and Free Radical Research Core of the University of Iowa. The 6,000 Curies cesium-137 gamma ray source model 81-16 calibrator (JL Shepherd and Associates, San Fernando, CA) delivered a total dose of 25 kGy of monoenergetic gamma radiation (0.667 MeV) to sterilize the samples before culture experiments.

Human retinal organoids were made from patient-derived induced pluripotent stem cells with genetic mutations congruent with retinal degeneration, as previously described. [35] Briefly, individual iPSC colonies derived from a donor with retinal degeneration were dissociated, passaged, and resuspended in 3D differentiation medium [DMEM (Gibco, Thermo Fisher Scientific, Grand Island, NY), 10% heat-inactivated human serum (innovative Research, Novi, MI), 20% CTS KnockOut Serum Replacement XenoFree medium (Gibco), 0.1 mM MEM non-essential amino acids (Gibco), 1 nM Sodium Pyruvate (Gibco), 0.1 mM 2-Mercaptoethanol (Gibco), 1% ECM (human type 1 and type 3 collagen/vitronectin/fibronectin, Advanced BioMatrix, Calsbad, CA), 20 mMY-27632 ROCK Inhibitor (EMD Millipore, Billerica, MA), 3nM IWR1e (Cayman

Chemical, Ann Arbor, MI), 3 M StemMACS CHIR (Miltenyi Biotec Inc., San Diego, CA), 100 nM SAG (Enzo Life Sciences, Farmingdale NY)]. The cells were plated in low-adherent 96-well sphere forming plates (Corning) at a density of 1 x 10^4 cells/well. Fresh 3D differentiation media was changed out every other day for 12 days to encourage sphere formation. On day 12, individual spheres were collected and transferred to 100 mm ultra-low adhesion plates. Spheres were left for an additional week to allow for differentiation in 3D differentiation media. On day 18, the sphere medium was switched to neural retina medium 1 [CTS KnockOut DMEM/F12 (Gibco), 2 mM GlutaMAX supplement (Gibco) and CTS N-2 supplement (Cell Therapy Systems, Thermo Fischer Scientific)] to promote differentiation into retina progenitor cells. After differentiating for 42 or 82 days, organoids were seeded onto the scaffolds.

Each sterilized PCLTA scaffold (~18 mm diameter) was laid flat in a 6 well culture dish, one scaffold per well. A sterile 10 mm cloning ring (Corning Inc.) was placed on top of each sample and scaffolds were subsequently coated with human laminin (50 μg/ml). Retinal organoids were deposited onto the scaffolds, inside the culture ring, at a density of 16 organoids/scaffold in 200 μl of cell culture media. Then, 2 mL of culture media was subsequently added to each well surrounding the cloning ring. At 48 hours post-seeding, cloning rings were removed and the media was replaced with fresh media. Scaffolds were fed every other day for 5 days before immunostaining.

Cells were fixed with 4% paraformaldehhyde and stained with goat biotinylated-anti-OTX2 (R&D Systems; 1:1000; Cat#: BAF1979), rabbit anti-Recoverin (EMD Millipore; 1:2000; Cat#: AB5585), and rabbit anti-TUJ1 (neuron-specific class III beta-tubulin; Sigma-Aldrich, St. Louis, MO; 1:1000; Cat#: T2200). The appropriate species-

specific, fluorescently-conjugated secondary antibodies were used to detect the primary antibodies: AlexaFluor goat anti-rabbit 568 (Cat#: A-11011) and AlexaFluor Streptavidin 647 (Cat#: S-21374). Nuclei were also stained with DAPI before observation with the EVOS FL Imaging System (Thermo Fisher Scientific) under appropriate fluorescence for image acquisition. Cells were counted using ImageJ thresholding and analyze particles functions.

4.3 Results

4.3.1 Threshold

The minimum length of time to form a PM gel and film was determined through trials of increasing exposure time at constant light intensities. Below the gel threshold, the resin was not observed to have crosslinked based on handling with forceps and was described a thin liquid. An increase in exposure time approached, first, the gel-forming threshold and then the film-forming threshold. The gel threshold was defined as the point when the resin first became cohesive and possible to hold with forceps after exposure. Gel samples were a solid that did not maintain a film shape when removed from the mold. The film-producing threshold was determined similarly to the gel threshold and was defined as the exposure time resulting in a solid that maintained its film structure once removed from the mold. The gel and film thresholds follow a similar trend: at low intensities, a longer exposure time was necessary to crosslink the polymer into a gel or film compared to higher light intensities (**Figure 4.1**). Both thresholds were fit with a nonlinear regression by the method of least squares.

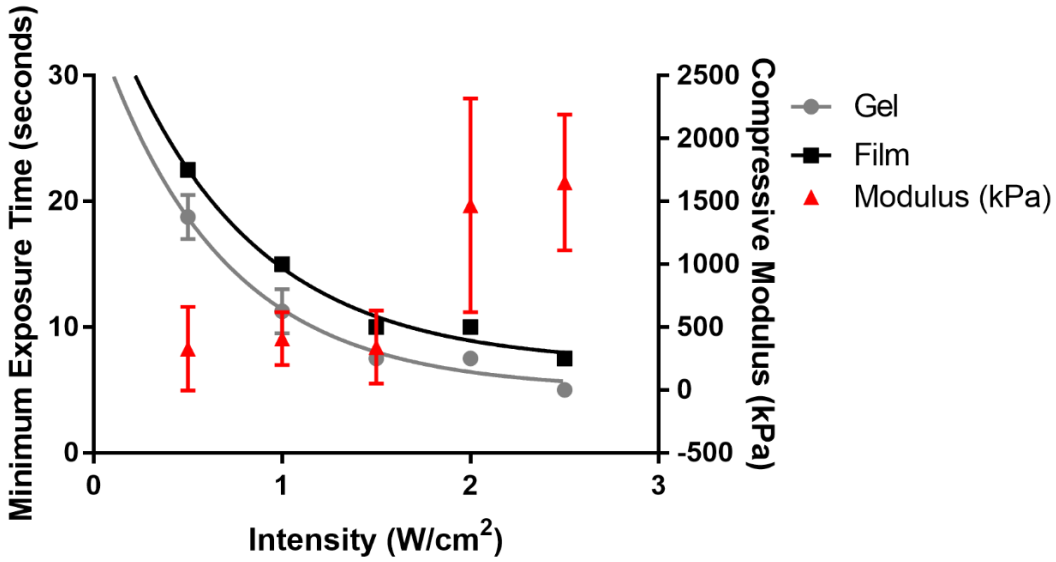

Figure 4.1: Thresholds and compressive modulus. The minimum required exposure time to form a gel or a film (gray and black, respectively) at a specific light intensity were determined and defined as the threshold. The compressive modulus was found for the threshold forming films (red) and is reported in kPa.

The compressive modulus was determined for films made at the threshold for each light intensity. While at lower intensities (0.5, 1.0, and 1.5 W/cm^3), films had similar moduli, each roughly 450 kPa, the elastic modulis of films created at higher intensities (1.5 and 2.0 W/cm^2) were greater, than the low intensity samples, each approximately 1600 kPa (**Figure 4.1**).However, it should be noted that the low and high intensity samples, as defined above, were analyzed on two separate days, calling into question the validity of these differences and the reliability of the selected testing method.

4.3.2 Pore Analysis

2D and 3D data about the pores in these PM PCLTA films was captured using confocal microscopy and the auto-fluorescence of PCLTA (**Figure 4.2A-F**). Samples created at the lowest intensity and highest exposure time in this study (0.5 W/cm^2 for 22.5 seconds) appear to have open, unclogged pores in both the volume rendering and pore profile analysis (**Figure 4.2A-B**). Narrowing of the average pore occurs at the middle of the film, followed by broadening toward the presumed bottom side. The overall thickness of the film is greater than anticipated at 116 μm. The middle intensity, 1.5 W/cm^2 for 10 seconds, also appeared to create open pores in the volume rendering; however, the average pore silhouette implies an hour-glass shape through the depth of the film, with a thin blockage in the middle (**Figure 4.2C-D**). The thickness of this sample, 125 μm, is also greater than the spacers used in fabrication. Lastly, the 2.5 W/cm^2 PM film, with an exposure time of 7.5 seconds, displayed a volume with unobstructed pores, yet the pore profile suggests a solid barrier in the middle of the depth of the pore (**Figure 4.2E-F**). Similar to other samples, the overall thickness of the highest intensity film was quantified as 110 μm. All the volume renderings suggest the pores are free of obstruction, but the analysis of the slices individually implies necking and eventual obstruction of the pores through the depth as the intensity increases and the exposure time decreases. The intensities studied between the values reported here follow the same pattern as those discussed in detail (**Figure 4.S1**).

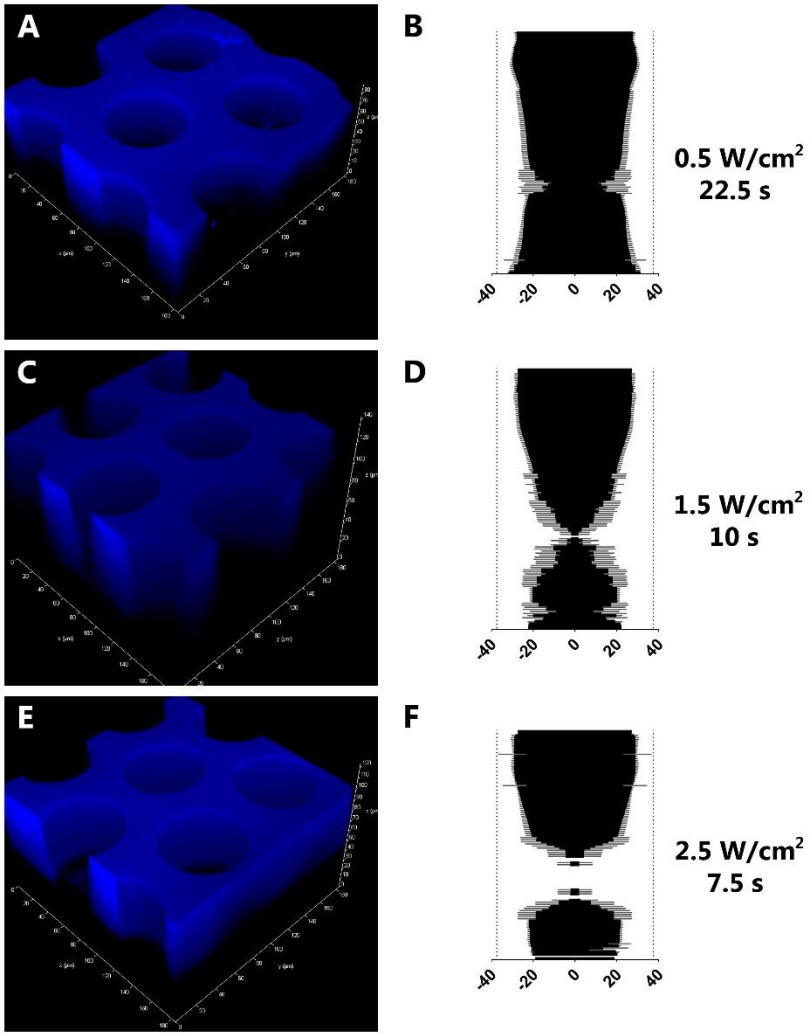

Figure 4.2: Confocal **m**icroscopy and **p**ore **p**rofiles. Lecia software acquired volume renderings of PM PCLTA at 0.5 W/cm^2 for 22.5 sec (**A**), 1.5 W/cm^2 for 10 sec (**C**), and 2.5 W/cm^2 for 7.5 sec (**E**). Silhouettes of the average pore diameter and standard deviation of each layer in the z-stack for the intensities and times previously listed (**B, D,** and **F**, respectively). There was a 1 μm step size between layers in the z-stack, the black labels the radius of the pore in each direction and the gray is the standard deviation.

Sterile films, polymerized at 1.5 W/cm^2 for 10 s, were loaded with retinal organoids to test cell loading and attachment. The 40 and 80 day retina organoids were not observably different; therefore one image was selected to represent both samples. A 2 mm biopsy punch of the PM PCLTA loaded with DAPI-stained cells (**Figure 4.3A**) displayed the seeding density possible from 16 organoids. The DAPI-stained nuclei were used to count the number of cells per unit area for both 40 and 80 day retinal organoids: 1,166 and 2,635 cells/mm^2, respectively.

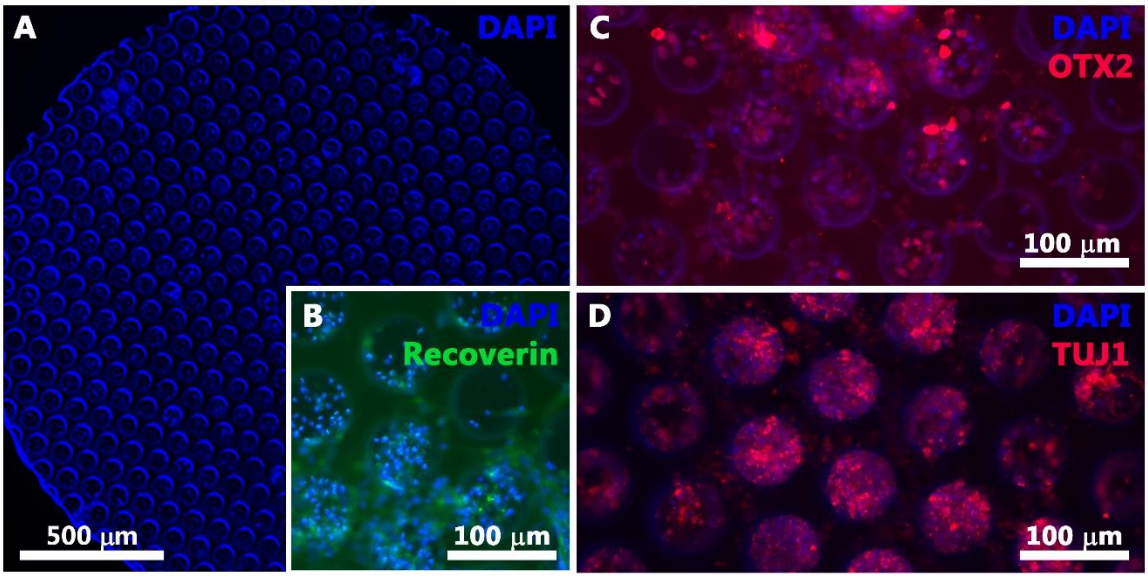

Figure 4.3: PM PCLTA loaded with retinal organoids. Eighty-day retinal organoid cells labeled with DAPI, a marker for DNA, on a 2 mm PM PCLTA scaffold (**A**). Retinal and neuronal markers were also observed: recoverin (**B**, 80 day), OTX2 (**C**, 80 day), and TUJ1 (**D**, 40 day).

Recoverin is a marker for photoreceptor cells, and there is minimal evidence of its presence in the seeded cells likely because they are still retinal progenitor cells (**Figure**

4.3B). The markers TUJ1 and OTX2 label molecules expressed in neurons and a transcription factor indicative of brain and sensory system development, respectively (**Figure 4.3C-D**). The cells appear to have maintained their neuronal and pre-retinal lineage through the cell seeding process and have densely filled the pores. The cells are believed to be inside of the pores, not just on the surface, due to their presence in focal planes other than at the surface.

4.4 Discussion

Two-dimensional PCLTA films are an advantageous alternative to two-photon polymerized scaffolds because of their quick fabrication time. We proposed development of this rapid fabrication technique to expedite the FDA approval process. If this less complex to produce scaffold can be established as a device first, then they may be used as a predicate device for two-photon polymerized scaffolds during the pursuit of regulatory approval. As such, optimized fabrication, formulation, and physical properties of PM PCLTA were examined as next steps in the pursuit of designing a cell replacement therapy to treat blindness.

The exposure time and light intensity have an inverse, nonlinear relationship: as the light intensity increases it requires less time to form crosslinks (**Figure 4.1**). At greater light intensities, photons penetrate the resin more effectively and excite more of the photoinitiator to create more free radicals per second. The greater this initaition activity, the more crosslinks are possible in a given timeframe. Therefore, a higher intensity requires less time to form the same relative number of crosslinks.

Compressive modulus at the different intensities and exposure times appeared to be grouped based on the day the data was collected (**Figure 4.1**). The sensitivity of the DMA may not be precise enough to detect differences in samples of this scale or minute differences throughout the film. For example, the compressive modulus of the PM PCLTA samples are hypothesized to vary based on their proximity to the pores and spacing between the pores. Interactions at the cellular level will likely be influenced by these microscale physical properties. Future analysis with an atomic force microscope, which uses a probe to detect differences on a micrometer scale, is more suitable to determine the modulus experienced at a cellular level.

Confocal microscopic analysis of the pores revealed the intensity and exposure time impacted shape of the pores when measured with ImageJ but not from the Lecia volume rendering software (**Figure 4.2**). All of the volumes observed from the image acquisition software appeared to have unobstructed pores. However, when each image of the stack was evaluated independently, the pores exhibit a narrowing of diameter as it extends midway through the film depth followed by expansion as it approaches the opposite side. The shape can be best described as an hour-glass silhouette. As the intensity increased, the diameter of the middle region shrank until it appeared to have closed off completely, followed by the same broadening as the pore approached the opposite surface of the film. The recorded thicknesses of all the films were greater than 100 μm when they were manufactured with a thickness of only 50 μm. Since the PCLTA auto-fluoresces, the acquired images require a longer exposure time or increased image brightness to be collected. This practice may have caused some artifacts in our image collection. We hypothesize that the thickness may be greater because the instrument is

picking up fluorescence out of the plane of view. To gather more specific fluorescence of the scaffold in future studies, a fluorescent label can either be bound to the surface or polymerized into the film. We expect that a more distinct labeling of the polymer will reduce the number of artifacts thought to be in our images. A conical shape approaching the midsection of the pore depth is hypothesized to be an accurate representation of the entire pore silhouette. Light bleeds laterally into the regions covered by the photomask by diffraction, causing the pores to narrow as they extend through the thickness of the film. At higher intensities, the constriction of the pores is more pronounced because the number of photons diffracting and polymerizing in these photomasked regions increases. The light intensity and exposure time combination selected for future work will be based on the film with the least shrinkage of the pores through its thickness.

Retinal organoid cells were loaded into the PM PCLTA scaffold readily, and they maintained their neuronal and pre-retinal lineage (**Figure 4.3**). These results are promising for transplantation of cell-loaded scaffolds in small animal models. Based on the seeding density of cells on these preliminary scaffolds, 1,166 and 2,635 cells per mm^2 are possible with the loading of 16 retinal organoids. The literature reports that as many as 80,000- 320,000 photoreceptor cells per mm^2 are found in a healthy eye,[36] we endeavor to approach this range through further investigation of the number of retinal organoids necessary to densely pack the scaffold and methods to dissociate them.

PM PCLTA has proven to be an efficient and simplified version of the two-photon PCLTA scaffolds. The pace at which studies of these films can be executed will allow this work to reach clinical trials more rapidly than their two-photon polymerized

counterparts. This will in turn, pave the way for the use of two-photon polymerized PCLTA scaffolds to mimic or replace even more intricate ocular tissues like the choroid.

4.5 Supplemental Information

Figure 4.S1: Complete comparison of PM PCLTA pores. Representative volume renderings at each intensity and exposure time examined in this study (**A**, **C**, **E**, **G**, **I**). Each image of the z-stack was taken 1 μm apart and analyzed individually to measure the average diameter of pores at that depth of the film. Pore profiles were constructed by plotting the average radius in each direction at the various depths of the film, with gray regions representing the standard deviation (**B**, **D**, **F**, **G**, **I**).

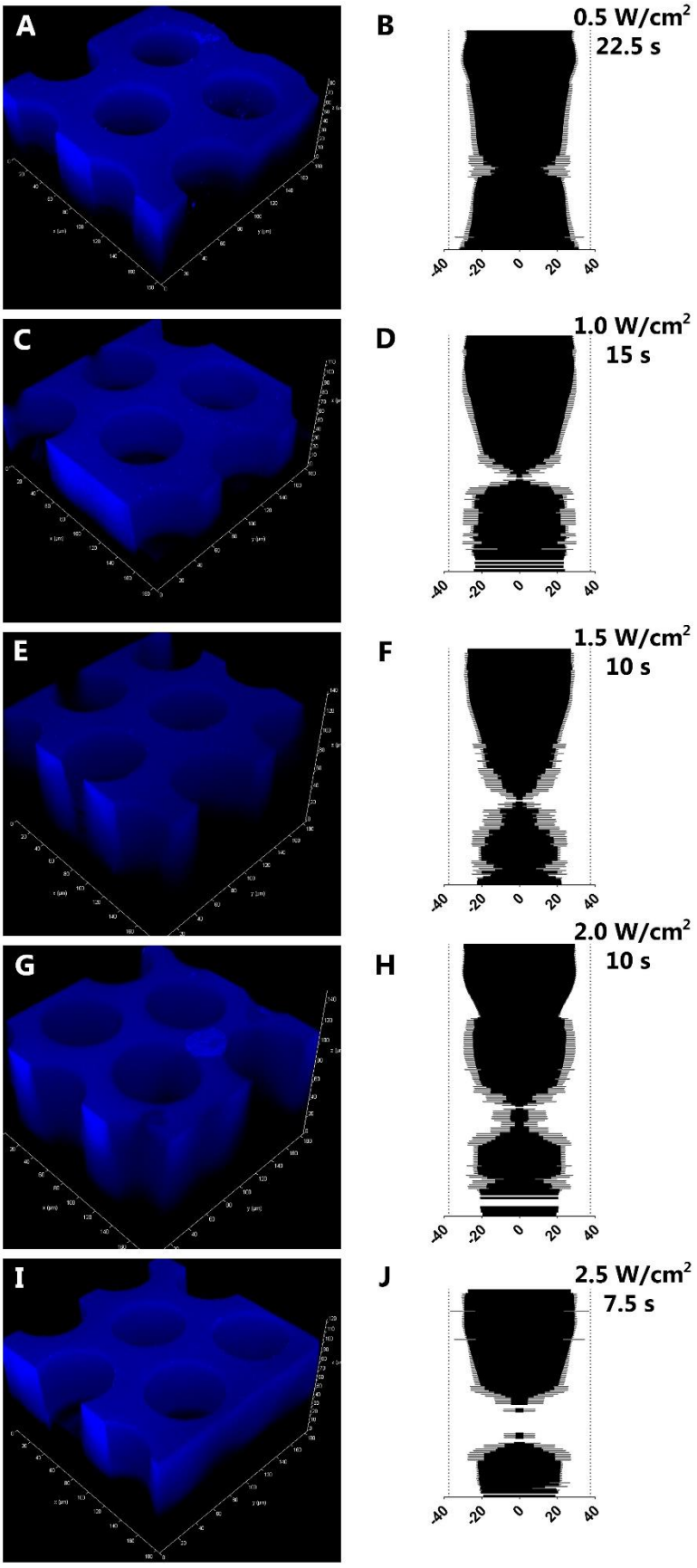

CHAPTER V: CONCLUSIONS AND FUTURE DIRECTIONS

5.1 Conclusions

Millions of patients with retinal degenerative diseases have few options when it comes to treating their debilitating visual impairment. Our proposed treatment to restore their vision is an autologous, genetically corrected transplant facilitated with a medical device. Namely, polymer support scaffolds are critical for cellular survival and integration in retinal cell replacement therapies. Some challenges in implementing a scaffold for this purpose include 1) selection of appropriate chemistry and 2) microstructural control for cell orientation and packing. Poly(caprolactone) is a good candidate material for retinal scaffolds, as it is biodegradable, biocompatible, and easily modified with reactive molecules. In this work, we optimized the conditions that contribute to photopolymerized PCL microstructure in order to create more effective and efficient retinal cell scaffolds.

Initially, we explored the use of two-photon polymerization (TPP) to 3D print our scaffold to achieve precise control. From the variety of functionalities and molecular weights of PCL explored, PCL triacrylated (PCLTA) with a molecular weight of 300 g/mol at a concentration of 75 wt% in dioxane was determined to have the best printing resolution. All of these molecular qualities: high degree of functionality, high concentration of molecules in solution, and low molecular weight, increased the concentration of reactive groups, resulting in the best model-to-printed-structure fidelity. The optimal printing parameters such as scanning speed, laser power, slicing distance, and hatching distance were also determined in order to produce the prototype scaffold (180 μm) that shrank the least, maintained pore qualities, and printed most efficiently.

Preliminary biocompatibility studies began as these results were still being interpreted, and an imperfect scaled-up scaffold was transplanted into the subretinal space of a porcine eye. The PCLTA device was well-tolerated in the retina and did not cause inflammation or infection in any tissues. However, at this point some drawbacks of this strategy emerged. First, the time to fabricate a scaffold for a pig or human study (5 mm disc) was estimated to take over a month. Thus, the time necessary to generate enough devices to pursue regulatory approval for clinical application became an obstacle. Secondly, the consistency of our synthesized PCLTA between batches was immeasurable because excess reactant in the product disguised the true success of the reaction. To address concerns of quality control of our PCLTA synthesis, methods to remove the excess reactants were explored. Washing with phase separations in concentrated sodium bicarbonate prevailed over washes with distilled water or elevated temperature rotary evaporation due to the salt providing a favorable chemical gradient for the acryloyl chloride to move toward the aqueous phase. The greater the degree of agitation, the more effective the washing method was because there was a greater surface area for the molecules to interact. The final synthesis method removed all evidence of the acryloyl chloride in the PCLTA, and a 60-70% substitution of acrylates onto the polymer was achieved.

As previously mentioned, the end goal of this work is to pursue clinical trials and treatments for retinal degeneration. Because it is the first device of its kind, the regulatory experiments to obtain Food and Drug Administration approval require a large number of devices and materials that would take a very long time to fabricate with TPP. Photomasked (PM) PCLTA films were studied as a rapid-to-fabricate alternative to the

TPP PCLTA in order to propel research on the safety and efficacy of a PCLTA photoreceptor cell scaffold. As such, the standards at which to produce these films were examined, varying the light intensity and exposure time used to make the scaffold. Preliminary results indicated that a higher intensity light necessitated less time under the UV light. This is due to the greater number of photons interacting with the specimen at high intensities achieving the same effect as more time at a lower intensity. Confocal observation and DMA quantification were utilized in an attempt to characterize the films made at the various intensities. However, these instruments were not sensitive enough to describe the PM PCLTA adequately. Retinal organoids were loaded onto the films to take a preliminary look into seeding density and loading methods. The cells maintained their retinal precursor lineage after one week on the PM PCLTA, and a density on the scale of 1,500 cells per mm^2 was achieved.

After rigorous experimentation of PCL with the purpose of discovering the best composition, concentration, and construction, the work to date shows promise to function as a tissue scaffold. Some future work that is necessary to achieve the purpose of this research includes: TPP fabrication of a 5 mm human photoreceptor scaffold, fluorescent tagging of TPP and PM PCLTA for confocal microscopy, physical characterization using atomic force microscopy (AFM), a protocol for sterilizing the device following International Organization for Standardization guidelines, and more extensive *in vitro* and *in vivo* studies.

5.2 Future Directions and Recommendations

The scale-up biocompatibility studies featured in Chapter II are of an imperfect prototype of the TPP PCLTA scaffold. Printing a new, fully developed human scale

scaffold with the optimized material, printing parameters, and scaffold design would prove overall success of all the work and determine the length of time necessary for fabrication. Additionally, study into the relationship between the size of the crosspores in computer generated model compared to the polymer scaffold should be explored to determine the relative amount of shrinkage in the z-direction. Once all of the pores are open, study of the crosspores as a design requirement should be pursued. Some metrics to measure necessity of the crosspores include: cell viability seeded in the device over time, chemical transport through the scaffold, and risk of cell migration laterally.

Both the TPP and PM PCLTA scaffolds could benefit from fluorescent labeling for confocal microscopic observation. Standard bright field microscopy does not have the resolution available to observe the scaffold microstructure, and scanning electron microscopy requires extensive drying, which damages the scaffolds in the process. Auto-fluorescence was determined not to be strong enough to remove artifacts in Chapter IV. As an alternative, selection of a fluorophore tag to attach to the surface or polymerize into the sample could remove these errors. Ideally, securing the tag to the surface of the PCLTA would be more favorable because it would not add a new chemical to the composition of the scaffold and potentially change qualities of the film or printed structure.

As mentioned in Chapter IV, DMA is not a reliable method for determining the modulus these scaffolds, as it cannot detect differences in physical properties experienced at a cellular level. Conversely, studying these properties with an atomic force microscope (AFM) would enable exploration of different moduli within PM or TPP PCL structures that occur due to the distance from the pore, concentration of polymer or photoinitiator,

and light dose. AFM also has impressive imaging capabilities to show surface texture and is gentle enough to image cells on the tissue scaffold. The use of AFM could improve the material design and composition such that the properties found in the natural retina could be approached.

In this work, two sterilization methods were used: washes with ethanol and sterile PBS were used before transplantation in Chapter II and a dose of 25 kGy of gamma irradiation was used to sterilize the scaffolds before in vitro studies in Chapter IV. An ethanol bath is not an approved or practical method of sterilization for clinical-grade materials, hence the shift toward irradiation. The highest level of radiation recommended by standard ISO 11137 was used to ensure the sterility of samples before a study into the minimum dose necessary to reach safe sterility levels. However, over-dosing the scaffold with radiation could cause an increase in crosslinks within the polymer network, changing the modulus and other possible mechanical properties. Future work should consider ISO guidelines and thorough sterility testing to determine the appropriate dose of radiation necessary for safety and preservation of the device.

General biocompatibility of crosslinked PCL scaffolds was demonstrated in both Chapters II and IV. However, there is far more in-depth work required to ensure safe interactions of both formulations (PM and TPP PCLTA) with human tissue. These include systemic toxicity analysis (underway for PM PCLTA) and characterization of degradation time and products, including their tolerance in various tissues. Furthermore, how and when cells are loaded onto the scaffolds must be studied to determine the best combination for cells to integrate into host tissue once transplanted. The age of retinal organoids at the point of seeding should be studied to discover when is the best time point

for promoting attachment to the scaffold and appropriate differentiation into rods and cones. Then, the length of time the retinal precursor cells are grown on the scaffold needs to be determined, as does the number of organoids necessary to fill the scaffold.

As presented in this thesis, precision biomaterials are the next step in personalized medicine. Here we have highlighted one example of their usefulness: in human retinal engineering. By modifying a biodegradable, synthetic polymer with slower dissolution times than traditional polymers used in biomaterials (e.g., PLGA), we have demonstrated one option for overcoming the challenge of retinal biomaterial chemistry. Using this chemistry, we also presented two fabrication methods (TPP and PM) that can be used to address a second obstacle to the realization of these devices: microstructural control. These results lay the groundwork for further refinement of retinal biomaterials. For example, photoreceptor cells represent just one layer of the retina that is affected by retinal degeneration and thus could benefit from replacement to restore vision in patients with late-stage retinal degeneration. Once this scaffold has been perfected, the technologies we have developed can be applied to other complex layers of the retina like the choroid, to other tissues, other applications including drug delivery devices or microfluidic biosensors.

REFERENCES

1. Choi, H. G.; Lee, M. J.; Lee, S. M., Visual impairment and risk of depression: A longitudinal follow-up study using a national sample cohort. *Sci Rep* **2018,** *8* (1), 2083.
2. Holz, F. G.; Strauss, E. C.; Schmitz-Valckenberg, S.; van Lookeren Campagne, M., Geographic atrophy: clinical features and potential therapeutic approaches. *Ophthalmology* **2014,** *121* (5), 1079-91.
3. Fernandez-Robredo, P.; Sancho, A.; Johnen, S.; Recalde, S.; Gama, N.; Thumann, G.; Groll, J.; Garcia-Layana, A., Current Treatment Limitations in Age-Related Macular Degeneration and Future Approaches Based on Cell Therapy and Tissue Engineering. *J Ophthalmol* **2014**.
4. Riera, M.; Fontrodona, L.; Albert, S.; Ramirez, D. M.; Seriola, A.; Salas, A.; Munoz, Y.; Ramos, D.; Villegas-Perez, M. P.; Zapata, M. A.; Raya, A.; Ruberte, J.; Veiga, A.; Garcia-Arumi, J., Comparative study of human embryonic stem cells (hESC) and human induced pluripotent stem cells (hiPSC) as a treatment for retinal dystrophies. *Mol Ther-Meth Clin D* **2016,** *3*.
5. Jinek, M.; East, A.; Cheng, A.; Lin, S.; Ma, E.; Doudna, J., RNA-programmed genome editing in human cells. *Elife* **2013,** *2*, e00471.
6. Mali, P.; Yang, L.; Esvelt, K. M.; Aach, J.; Guell, M.; DiCarlo, J. E.; Norville, J. E.; Church, G. M., RNA-guided human genome engineering via Cas9. *Science* **2013,** *339* (6121), 823-6.
7. MacLaren, R. E.; Pearson, R. A.; MacNeil, A.; Douglas, R. H.; Salt, T. E.; Akimoto, M.; Swaroop, A.; Sowden, J. C.; Ali, R. R., Retinal repair by transplantation of photoreceptor precursors. *Nature* **2006,** *444* (7116), 203-7.
8. Santos-Ferreira, T.; Volkner, M.; Borsch, O.; Haas, J.; Cimalla, P.; Vasudevan, P.; Carmeliet, P.; Corbeil, D.; Michalakis, S.; Koch, E.; Karl, M. O.; Ader, M., Stem Cell-Derived Photoreceptor Transplants Differentially Integrate Into Mouse Models of Cone-Rod Dystrophy. *Invest Ophthalmol Vis Sci* **2016,** *57* (7), 3509-20.
9. Worthington, K. S.; Wiley, L. A.; Bartlett, A. M.; Stone, E. M.; Mullins, R. F.; Salem, A. K.; Guymon, C. A.; Tucker, B. A., Mechanical properties of murine and porcine ocular tissues in compression. *Exp Eye Res* **2014,** *121*, 194-199.
10. Tomita, M.; Lavik, E.; Klassen, H.; Zahir, T.; Langer, R.; Young, M. J., Biodegradable polymer composite grafts promote the survival and differentiation of retinal progenitor cells. *Stem Cells* **2005,** *23* (10), 1579-1588.
11. Tao, S.; Young, C.; Redenti, S.; Zhang, Y.; Klassen, H.; Desai, T.; Young, M. J., Survival, migration and differentiation of retinal progenitor cells transplanted on micro-machined poly(methyl methacrylate) scaffolds to the subretinal space. *Lab on a chip* **2007,** *7* (6), 695-701.
12. Redenti, S.; Neeley, W. L.; Rompani, S.; Saigal, S.; Yang, J.; Klassen, H.; Langer, R.; Young, M. J., Engineering retinal progenitor cell and scrollable poly(glycerol-sebacate) composites for expansion and subretinal transplantation. *Biomaterials* **2009,** *30* (20), 3405-3414.
13. Yao, J.; Ko, C. W.; Baranov, P. Y.; Regatieri, C. V.; Redenti, S.; Tucker, B. A.; Mighty, J.; Tao, S. L.; Young, M. J., Enhanced Differentiation and Delivery of Mouse Retinal Progenitor Cells Using a Micropatterned Biodegradable Thin-Film Polycaprolactone Scaffold. *Tissue Eng Pt A* **2015,** *21* (7-8), 1247-1260.

14. Yao, J.; Tao, S. L.; Young, M. J., Synthetic Polymer Scaffolds for Stem Cell Transplantation in Retinal Tissue Engineering. *Polymers-Basel* **2011,** *3* (2), 899-914.
15. Tucker, B. A.; Redenti, S. M.; Jiang, C.; Swift, J. S.; Klassen, H. J.; Smith, M. E.; Wnek, G. E.; Young, M. J., The use of progenitor cell/biodegradable MMP2-PLGA polymer constructs to enhance cellular integration and retinal repopulation. *Biomaterials* **2010,** *31* (1), 9-19.
16. Rodriguez Villanueva, J.; Rodriguez Villanueva, L., Turning the screw even further to increase microparticle retention and ocular bioavailability of associated drugs: The bioadhesion goal. *Int J Pharm* **2017,** *531* (1), 167-178.
17. Huang, S. F.; Chen, J. L.; Yeh, M. K.; Chiang, C. H., Physicochemical properties and in vivo assessment of timolol-loaded poly(D,L-lactide-co-glycolide) films for long-term intraocular pressure lowering effects. *J Ocul Pharmacol Ther* **2005,** *21* (6), 445-53.
18. Kehoe, S.; Zhang, X. F.; Lewis, L.; O'Shea, H.; Boyd, D., Characterization of PLGA based composite nerve guidance conduits: effect of F127 content on modulus over time in simulated physiological conditions. *J Mech Behav Biomed Mater* **2012,** *14*, 180-5.
19. Middleton, J. C.; Tipton, A. J., Synthetic biodegradable polymers as orthopedic devices. *Biomaterials* **2000,** *21* (23), 2335-2346.
20. Rai, B.; Teoh, S. H.; Hutmacher, D. W.; Cao, T.; Ho, K. H., Novel PCL-based honeycomb scaffolds as drug delivery systems for rhBMP-2. *Biomaterials* **2005,** *26* (17), 3739-3748.
21. Woodruff, M. A.; Hutmacher, D. W., The return of a forgotten polymer-Polycaprolactone in the 21st century. *Prog Polym Sci* **2010,** *35* (10), 1217-1256.
22. Lee, K. H.; Kim, H. Y.; Khil, M. S.; Ra, Y. M.; Lee, D. R., Characterization of nano-structured poly(epsilon-caprolactone) nonwoven mats via electrospinning. *Polymer* **2003,** *44* (4), 1287-1294.
23. Zein, I.; Hutmacher, D. W.; Tan, K. C.; Teoh, S. H., Fused deposition modeling of novel scaffold architectures for tissue engineering applications. *Biomaterials* **2002,** *23* (4), 1169-1185.
24. Christiansen, A. T.; Tao, S. L.; Smith, M.; Wnek, G. E.; Prause, J. U.; Young, M. J.; Klassen, H.; Kaplan, H. J.; la Cour, M.; Kiilgaard, J. F., Subretinal Implantation of Electrospun, Short Nanowire, and Smooth Poly(epsilon-caprolactone) Scaffolds to the Subretinal Space of Porcine Eyes. *Stem Cells Int* **2012**.
25. Calejo, M. T.; Ilmarinen, T.; Vuorimaa-Laukkanen, E.; Talvitie, E.; Hakola, H. M.; Skottman, H.; Kellomaki, M., Langmuir-Schaefer film deposition onto honeycomb porous films for retinal tissue engineering. *Acta Biomater* **2017,** *54*, 138-149.
26. Sorkio, A.; Porter, P. J.; Juuti-Uusitalo, K.; Meenan, B. J.; Skottman, H.; Burke, G. A., Surface Modified Biodegradable Electrospun Membranes as a Carrier for Human Embryonic Stem Cell-Derived Retinal Pigment Epithelial Cells. *Tissue Eng Part A* **2015,** *21* (17-18), 2301-14.
27. Worthington, K. S.; Wiley, L. A.; Kaalberg, E. E.; Collins, M. M.; Mullins, R. F.; Stone, E. M.; Tucker, B. A., Two-photon polymerization for production of human iPSC-derived retinal cell grafts. *Acta Biomater* **2017,** *55*, 385-395.
28. Worthington, K. S.; Wiley, L. A.; Kaalberg, E. E.; Collins, M. M.; Mullins, R. F.; Stone, E. M.; Tucker, B. A., Two-photon polymerization for production of human iPSC-derived retinal cell grafts. *Acta Biomater* **2017,** *55*, 385-395.

29. Ross, J. W.; Fernandez de Castro, J. P.; Zhao, J.; Samuel, M.; Walters, E.; Rios, C.; Bray-Ward, P.; Jones, B. W.; Marc, R. E.; Wang, W.; Zhou, L.; Noel, J. M.; McCall, M. A.; DeMarco, P. J.; Prather, R. S.; Kaplan, H. J., Generation of an inbred miniature pig model of retinitis pigmentosa. *Invest Ophthalmol Vis Sci* **2012,** *53* (1), 501-7.
30. Scott, P. A.; de Castro, J. P.; DeMarco, P. J.; Ross, J. W.; Njoka, J.; Walters, E.; Prather, R. S.; McCall, M. A.; Kaplan, H. J., Progression of Pro23His Retinopathy in a Miniature Swine Model of Retinitis Pigmentosa. *Transl Vis Sci Technol* **2017,** *6* (2), 4.
31. Sohn, E. H.; Jiao, C.; Kaalberg, E.; Cranston, C.; Mullins, R. F.; Stone, E. M.; Tucker, B. A., Allogenic iPSC-derived RPE cell transplants induce immune response in pigs: a pilot study. *Sci Rep* **2015,** *5*, 11791.
32. Worthington, K. S.; Wiley, L. A.; Bartlett, A. M.; Stone, E. M.; Mullins, R. F.; Salem, A. K.; Guymon, C. A.; Tucker, B. A., Mechanical properties of murine and porcine ocular tissues in compression. *Exp Eye Res* **2014,** *121*, 194-9.
33. Cai, L.; Wang, S. F., Poly(epsilon-caprolactone) acrylates synthesized using a facile method for fabricating networks to achieve controllable physicochemical properties and tunable cell responses. *Polymer* **2010,** *51* (1), 164-177.
34. Worthington, K. S.; Green, B. J.; Rethwisch, M.; Wiley, L. A.; Tucker, B. A.; Guymon, C. A.; Salem, A. K., Neuronal Differentiation of Induced Pluripotent Stem Cells on Surfactant Templated Chitosan Hydrogels. *Biomacromolecules* **2016,** *17* (5), 1684-1695.
35. Wiley, L. A.; Burnight, E. R.; DeLuca, A. P.; Anfinson, K. R.; Cranston, C. M.; Kaalberg, E. E.; Penticoff, J. A.; Affatigato, L. M.; Mullins, R. F.; Stone, E. M.; Tucker, B. A., cGMP production of patient-specific iPSCs and photoreceptor precursor cells to treat retinal degenerative blindness. *Sci Rep* **2016,** *6*, 30742.
36. Curcio, C. A.; Sloan, K. R., Packing geometry of human cone photoreceptors: variation with eccentricity and evidence for local anisotropy. *Vis Neurosci* **1992,** *9* (2), 169-80.